Semideterministic quantum dot placement in heteroepitaxy

Wang, Z.; Bouwmeester, D.

Citation

Wang, Z., & Bouwmeester, D. (2025). Semideterministic quantum dot placement in heteroepitaxy. *Physical Review Applied*, *24*(5). doi:10.1103/4wzh-hbgl

PHYSICAL REVIEW APPLIED **24,** 054072 (2025)

Semideterministic quantum dot placement in heteroepitaxy

Zihang Wang[1,*] and Dirk Bouwmeester[1,2]

[1] *Department of Physics, University of California Santa Barbara, Santa Barbara, California 93106, USA*
[2] *Huygens-Kamerlingh Onnes Laboratory, Leiden University, P.O. Box 9504, 2300 RA Leiden, Netherlands*

(Received 7 July 2025; revised 26 September 2025; accepted 6 November 2025; published 24 November 2025)

Achieving deterministic placement of self-assembled quantum dots (QDs) during epitaxial growth is essential for the reliable and efficient fabrication of high-quality single-photon sources and solid-state cavity quantum electrodynamics (cQED) systems, yet it remains a significant challenge, owing to the inherent stochasticity of QD nucleation processes. In this work, we theoretically and numerically demonstrate that deterministic QD nucleation within a pristine growth region, e.g., InAs on a (001)-oriented GaAs substrate, can be achieved by engineering the boundary geometry of that region. During epitaxial growth, adatoms initially move toward the boundary and promote the formation of primary QDs along the boundary, driven by curvature and diffusion anisotropy. The resulting primary QD distribution will generate many-body interactions that dynamically reshape the chemical potential landscape for subsequently deposited adatoms, enabling the formation of secondary QDs within the pristine growth region. These findings provide a theoretical foundation for reliable patterning of high optical-quality QDs, with potential applications in next-generation quantum photonic devices.

DOI: 10.1103/4wzh-hbgl

I. INTRODUCTION

Self-assembled semiconductor quantum dots (QDs) play a central role in on-chip quantum optics devices. Integrating QDs with optical microcavities, such as photonic crystals [1–3], microdisks [4], and micropillars [5–8], results in cavity quantum electrodynamics (cQED) systems capable of generating single photons on demand in a single optical mode via the Purcell effect. This capability is essential for implementing quantum cryptographic schemes and quantum communication networks [9–11].

With additional single electron charge control, QDs can be used to entangle photons with electron spins [12–16], enabling coherent transfer of quantum states between spin and photonic degrees of freedom [17,18]. Such coherent light-matter interactions at the single quantum level are essential for establishing distributed entanglement across quantum networks [19]. Recent achievements include the deterministic on-chip generation of spin photon entanglement in QDs [20]; optical polarization and cooling of nuclear spin ensembles via the optical driving of a charged QD, enabling access and control at the single spin level [21]; and the high-efficiency generation of spin photon entangled states, a critical capability for future quantum repeater architectures [22].

The scaling of this semiconductor technology platform is, however, hampered by the fact that self-assembled QDs nucleate at random locations on the surface during molecular beam epitaxy (MBE). As a result, either microcavities must be carefully fabricated around precharacterized QD locations (e.g., Refs. [23,24]) or postselection must be used to identify devices in which a QD happens to be well aligned with the cavity mode.

To avoid this time- and resource-consuming approach, several attempts have been made to implement prepatterned templates, such as those generated by buried stressors [25,26] and capping layers [27,28], to control adatom migration so that QD nucleation occurs at predetermined locations. However, the accuracy with which these locations can be predicted is still influenced by surface asymmetric diffusion, strain resulting from lattice mismatch or surface imperfections, and the precise growth parameters [29–32]. The interplay of these effects remains largely unexplored, especially in efforts to predict spatial distributions of QDs under realistic growth conditions [33,34].

Coarse-grained models have captured qualitative features observed in experiments. For example, kinetic Monte Carlo (KMC) simulations have demonstrated how prepatterned substrates can direct and control nucleation sites [35]; phase-field simulations have reproduced QD densities comparable to experimental results on flat surfaces and have shown that surface patterns can guide QD nucleation, leading to more ordered dot placement [36].

While these theoretical models successfully capture the qualitative modulation of QD density resulting from strain fields, the role of spatiotemporal correlations in QD

---

[*] Contact author: zihangwang@ucsb.edu

distributions, such as conditioning on previously formed QDs, has not yet been theoretically addressed.

We propose an overdamped Langevin framework, demonstrating that semideterministic QD placement is theoretically achievable through the combined effects of geometry-defined boundary profiles and the secondary fields generated by previously nucleated QDs along the boundary. These boundary-anchored QDs dynamically reshape the chemical potential landscape, significantly modifying the diffusion kinetics of newly deposited adatoms. This results in secondary QD formation on the pristine region within the boundaries. This stochastic formalism provides a comprehensive model for the semideterministic spatial organization of QDs, opening new avenues for constructing spatially ordered cQED systems for scalable quantum networks.

II. ADATOM DENSITY AND QD NUCLEATION IN THE QUASISTATIONARY LIMIT

In traditional heteroepitaxy, atoms are deposited onto a planar substrate with effective boundaries at infinity, under homogeneous temperature and stress conditions. The spatial adatom density is typically approximated as translationally invariant. As a result, nucleation sites are uniformly distributed across the entire substrate. QD nucleation typically occurs via the Stranski-Krastanov (SK) growth mode [37,38]. This mode is one of the three primary epitaxial growth modes observed in thin-film deposition and is particularly relevant in heteroepitaxy where two different materials are involved (e.g., InAs on GaAs) [39]. It describes a transition from two-dimensional (2D) layer-by-layer growth to three-dimensional (3D) island formation. When deposition begins, the adatoms initially form a thin flat wetting layer on the substrate surface. This layer grows coherently, adopting the lattice constant of the underlying substrate, despite a lattice mismatch. As the wetting layer thickens, strain energy accumulates, owing to lattice mismatch between the film and the substrate (e.g., InAs has an approximately 7% larger lattice constant than GaAs) [40]. After reaching a critical thickness, typically a few monolayers, local instabilities are induced to release strain energy elastically, triggering spontaneous formation of symmetric three-dimensional islands [41]. Adatoms begin to aggregate at these energetically favorable sites, forming nanometer-sized clusters (QDs) that are stable (self-limited in size) and exhibit various morphologies and transitions, such as the pyramid-to-dome transition, which have been observed and investigated both experimentally and theoretically [42–44]. As more adatoms are introduced in the system, coherent (elastic) QD growth becomes metastable and incoherent (plastic) growth mechanisms, such as dislocation formation, ripening, and the adoption of elongated island shapes [41,45], emerge. In this work, we focus on the coherent QD growth regime within the pristine surface, where QDs are considered to be dislocation-free and adopt symmetric shapes on the wetting layer.

While the proposed theoretical framework is, in general, applicable to any substrate with arbitrary orientation, we address specifically the standard SK growth mode of InAs on the GaAs (001)-$\beta_2(2 \times 4)$ surface [46]: arsenic (As) adatoms tend to form surface dimers on attachment, resulting in dimer row or valley structures. Indium (In) atoms diffuse with significantly different rates, depending on whether their motion with respect to the As dimer rows [47] is tangential, which is slower and aligned along $\hat{\mathbf{y}} \equiv [110]$, or orthogonal, which is faster and aligned along $\hat{\mathbf{x}} \equiv [1\bar{1}0]$. This biaxial anisotropy is governed by a rank-2 diffusion tensor, which results in elongated quantum dots aligned along the fast diffusion axis $[1\bar{1}0]$ [48]. In this work, we assume that the diffusion tensor is dominated by its diagonal components, although, in general, nonzero off-diagonal terms can contribute to surface diffusion, depending on the substrate crystallographic orientation, adatom species, and temperature.

As suggested from several recent experimental studies, the introduction of boundary fields may arise from local strain gradients, such as those generated by buried stressors [25,26] and capping layers [27,28], or from thermal gradients across a substrate. As illustrated in Fig. 1, we present several examples of boundary fields, which can be parametrized by either arc length or the shape of composite geometries. We classify boundary fields into three types: exterior, interior, and soft boundary fields. Both exterior and interior fields correspond to hard physical boundaries (for example, hard mask edges) that adatoms cannot physically penetrate during the epitaxy process. In contrast, a soft boundary field, such as one induced by buried stressors, is associated with partially forbidden regions where adatom migration is energetically unfavorable during growth, for example, in regions exhibiting thermal or strain gradients. Boundary field strengths, governed by in-plane compressive strain and local impurities, can alter the diffusion dynamics of adatoms during epitaxy, resulting in an increased likelihood of quantum dot nucleation within or near the defined boundary region. We refer to the exposed pristine surface (white-colored regions in Fig. 1) as the bulk.

The dynamics of the adatom density field are governed by the two-dimensional continuity equation, which relates the temporal change in density to the divergence of the adatom flux:

$$\partial_t n(\mathbf{r}, t) + \nabla \cdot \mathbf{J}(\mathbf{r}, n, B, t) = 0, \tag{1}$$

where $\mathbf{J}(\mathbf{r}, n, B, t)$ is the local adatom current density, $\mathbf{r}$ is the spatial coordinate vector, t is time, and $B = \int du\, B[\mathbf{r} - \mathbf{r}_{\mathrm{bd}}(u)]$ represents the spatially varying boundary field strength at $\mathbf{r}$. The boundary field is parameterized by u, the

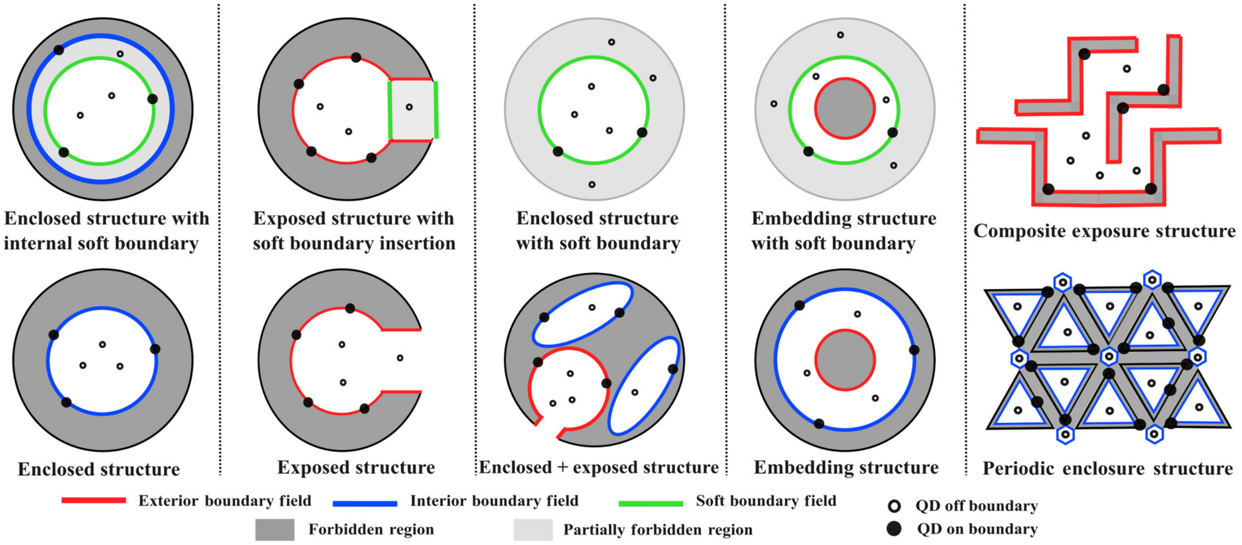

FIG. 1. Patterned geometries used to generate engineered boundary fields (e.g., strain fields). Red and blue lines indicate the boundary contours of patterned regions that induce localized field gradients. For illustrative purposes, solid black circles represent quantum dots (QDs) nucleating directly at these boundaries, while open circles denote QDs formed under the collective influence of both the boundary fields and QDs already formed on the boundary. Various pattern geometries demonstrate the flexibility of geometric design in controlling the spatial distribution of boundary-induced QD nucleation. The dark gray regions represent areas that adatoms cannot physically access, such as hard masks (forbidden regions), while light gray regions denote areas where adatom access is energetically unfavorable (partially forbidden). In this work, we refer to the exposed pristine surface (white regions) as the bulk.

arc-length variable along the boundary, and $\mathbf{r}_{\text{bd}}(u)$ denotes the unit-speed spatial parametrization of the boundary at u. We note that, in general, the boundary field is a tensor that captures structural coupling within the boundary contour. Without loss of generality of our method, we assume that $B[\mathbf{r}-\mathbf{r}_{\text{bd}}(u)]$ is a scalar field.

The current density (flux) $\mathbf{J}(\mathbf{r}, n, B, t)$ can be decomposed into two contributions: the lateral current density $\mathbf{J}_{\text{lateral}}$ and the vertical current density $\mathbf{J}_{\text{vertical}}$, representing, respectively, in-plane adatom diffusion and out-of-plane deposition or desorption. In the quasistationary limit, the epitaxy rate at a given site $\mathbf{r}$ is much smaller than the lateral diffusion rate, such that

$$|\mathbf{J}_{\text{vertical}}| \approx \lambda n + J_{\text{dep}}\left(\sum_{m=-\infty}^{\infty}\delta\left(t-m\,t_{\text{dep}}\right)\right) \ll |\mathbf{J}_{\text{lateral}}|, \tag{2}$$

where λ is the constant desorption rate, t_{dep} is the period between subsequent depositions, and J_{dep} is the deposition flux magnitude. This leads to a separation of fast and slow timescales: the lateral adatom density equilibrates rapidly, while the source and sink terms in the continuity equation associated with deposition or desorption act only as slowly varying perturbations.

In the quasistationary limit, where $\mathbf{J}(\mathbf{r}, n, B, t) \approx \mathbf{J}_{\text{lateral}}$, the lateral evolution of the adatom density is governed by the coupled dynamics of the local adatom density $n(\mathbf{r})$ and the associated lateral current density $\mathbf{J}$, which can be described by a quasiequilibrium Boltzmann distribution:

$$P[n, \mathbf{J}] = \frac{1}{\mathcal{Z}}\exp\left[-\frac{1}{k_B T}H[n, \mathbf{J}, B]\right], \tag{3}$$

where $H[n(\mathbf{r}), \mathbf{J}(\mathbf{r}), B]$ is a general many-body correlation functional associated with the configuration $[n, \mathbf{J}]$ and $\mathcal{Z}$ is the partition function $\mathcal{Z} = \int \mathcal{D}n\mathcal{D}\mathbf{J}\exp[-H/k_B T]$, integrated over all admissible field configurations.

The QD nucleation probability at a site $\mathbf{r}$ depends on the ensemble average over all density and current fields, and takes the form

$$P_{\text{QD}}(\mathbf{r}) = \frac{1}{\mathcal{Z}}\int \mathcal{D}n\,\mathcal{D}\mathbf{J}\;P[n, \mathbf{J}]\cdot\nu\left(n(\mathbf{r}), \mathbf{J}(\mathbf{r})\right), \tag{4}$$

where $\nu(n(\mathbf{r}), \mathbf{J}(\mathbf{r}))$ is the local nucleation rate function, modeled as

$$\nu(n, \mathbf{J}) = \nu_0\cdot\Theta\left(n - n_{\text{seed}}\right)\cdot\mathcal{R}(n, \mathbf{J}), \tag{5}$$

with n_{seed} denoting the lowest adatom density (subcritical density) that initiates the QD nucleation process at a given site; Θ is the Heaviside step function and $\mathcal{R}(n, \mathbf{J})$ is a modulation factor that may be modeled as either a delta function $\delta(n - n_{\text{seed}})$ or a smooth exponential dependence on n and $\mathbf{J}$.

While this expression for the nucleation probability is formally exact in the quasistationary limit, the high-dimensional structure of the functional renders analytical treatment infeasible in most practical scenarios.

Direct sampling of the distribution $P[n, \mathbf{J}]$ is computationally intractable, owing to nonlocal correlations and nonlinear coupling between the adatom density $n(\mathbf{r})$ and flux $\mathbf{J}(\mathbf{r})$ embedded in the functional $H[n, \mathbf{J}, B]$. Consequently, conventional importance-sampling methods are often inefficient or unstable. To overcome this challenge, we adopt a stochastic sampling approach based on Langevin dynamics, which enables Monte Carlo sampling of field configurations according to the Boltzmann weight $\exp[-H[n, \mathbf{J}, B]/(k_B T)]$. In this framework, the time evolution of $n(\mathbf{r}, t)$ and $\mathbf{J}(\mathbf{r}, t)$ is governed by coupled Langevin equations that incorporate both deterministic drift toward the minimum of $H[n, \mathbf{J}, B]$ and stochastic noise consistent with thermal fluctuations, in accordance with the fluctuation-dissipation theorem [49]. The steady-state solution of the corresponding Fokker-Planck equation yields the quasistationary distribution $P[n, \mathbf{J}]$ [50]. This approach allows efficient exploration of the high-dimensional field space and accurate estimation of ensemble-averaged observables, including the spatially resolved QD nucleation probability $P_{\mathrm{QD}}(\mathbf{r})$.

III. EMPIRICAL FIELD, QD NUCLEATION, AND LANGEVIN-BASED MONTE CARLO SAMPLING

To sample the quasistationary field configurations from $P[n, \mathbf{J}]$, we introduce a discrete empirical adatom density field $\hat{n}(\mathbf{r}, t)$ and empirical current density $\hat{\mathbf{J}}(\mathbf{r}, t)$, defined as sums over Dirac delta functions centered on an ensemble of adatoms $\{\mathbf{r}_i\}$, where each adatom is labeled by an index i,

$$\hat{n}(\mathbf{r}, t) = \sum_{i=1}^{N} \delta\left(\mathbf{r} - \mathbf{r}_i(t)\right),$$
$$\hat{\mathbf{J}}(\mathbf{r}, t) = \sum_{i=1}^{N} \frac{d\mathbf{r}_i(t)}{dt}\, \delta\left(\mathbf{r} - \mathbf{r}_i(t)\right), \tag{6}$$

which satisfy the continuity equation by construction. We emphasize that “empirical” here denotes a representation of the exact microscopic configuration, constructed without any coarse-graining.

We assume that adatoms are initially deposited uniformly onto the surface Ω, so that $\hat{n}(\mathbf{r}, 0) \approx 1/\Omega$, with Ω being the surface area, and each adatom i undergoes stochastic evolution governed by the following overdamped Langevin dynamics ($k_B T \equiv 1$):

$$m \frac{d^2\mathbf{r}_i}{dt^2} \approx 0 = -\mathbf{\Gamma}\, \frac{d\mathbf{r}_i}{dt} - \nabla_i U_{\mathrm{sys}} + \sqrt{2\,\mathbf{\Gamma}}\; \boldsymbol{\eta}_i(t), \tag{7}$$

where m is the effective mass, $\mathbf{\Gamma}$ is the friction tensor (assumed diagonal) along the two principal crystallographic directions $[1\bar{1}0]$ and $[110]$, and $\boldsymbol{\eta}_i(t)$ is a Gaussian noise term (a “distribution”) with statistics $\langle \eta_i(t)\, \eta_j(t') \rangle = \delta_{ij}\, \delta(t - t')$.

The total microscopic potential energy U_{sys} includes both the boundary field B and repulsive pairwise adatom interaction w, defined as a functional of the empirical adatom density field over the entire exposed substrate area Ω:

$$U_{\mathrm{sys}}[\hat{n}] = \int du \int_{\Omega} B[\mathbf{r} - \mathbf{r}_{\mathrm{bd}}(u)]\, \hat{n}(\mathbf{r}, t)\, d\mathbf{r} + \frac{1}{2} \iint_{\Omega} \hat{n}(\mathbf{r}, t)\, w(\mathbf{r} - \mathbf{r}')\, \hat{n}(\mathbf{r}', t)\, d\mathbf{r}\, d\mathbf{r}'. \tag{8}$$

By summing over all adatoms i, the empirical density field evolves according to the following stochastic differential equation (SDE):

$$\frac{\partial \hat{n}(\mathbf{r}, t)}{\partial t} = \nabla \cdot \left[\hat{n}(\mathbf{r}, t)\mathbf{D}\nabla \mu(\mathbf{r}, t)\right] + \nabla \cdot \left[\sqrt{2\hat{n}(\mathbf{r}, t)\mathbf{D}}\, \boldsymbol{\eta}(\mathbf{r}, t)\right], \tag{9}$$

where the diffusion tensor is given by $\mathbf{D} = \mathbf{\Gamma}^{-1}$ and the functional derivative $\mu = \delta U_{\mathrm{sys}}/\delta \hat{n}(\mathbf{r}, t)$ represents the single-adatom chemical potential landscape as the sum of a boundary-induced term and pairwise interaction contributions:

$$\mu(\mathbf{r}, t) = \int du\, B\left[\mathbf{r} - \mathbf{r}_{\mathrm{bd}}(u)\right] + \int_{\Omega} w\left(\mathbf{r} - \mathbf{r}'\right)\, \hat{n}(\mathbf{r}', t)\, d\mathbf{r}'. \tag{10}$$

The spatial gradient of this chemical potential landscape, $\mathbf{F}(\mathbf{r}, t) = -\nabla \mu(\mathbf{r}, t)$, corresponds to the microscopic force acting on the adatom ensemble. While the functional derivative $\mu = \delta U_{\mathrm{sys}}/\delta \hat{n}(\mathbf{r}, t)$ is not rigorously defined, owing to the singular nature of $\hat{n}$, which consists of Dirac delta functions, in practice, the values and gradients of $\mu(\mathbf{r}, t)$ are computed directly from the adatom-level Langevin dynamics. Thus, Eq. (9) should be interpreted as describing the stochastic evolution of an adatom ensemble, rather than as a coarse-grained partial differential equation (PDE).

To sample the density field $\hat{n}(\mathbf{r}, t)$, we do not solve Eq. (9) directly. Instead, we simulate Langevin dynamics for an ensemble of N adatoms and estimate the empirical field via a grid-based Monte Carlo technique. Specifically, we evolve the single-adatom Langevin equation given in Eq. (7),

$$\frac{d\mathbf{r}_i}{dt} = -\mathbf{D}\nabla_i U_{\mathrm{sys}} + \sqrt{2\,\mathbf{D}}\; W_i(t), \tag{11}$$

where $W_i(t)$ is a standard Wiener process. From the resulting trajectories, the empirical adatom density field is computed by counting particles on a spatial grid element $\mathrm{d}\Omega$, parametrized by the two-dimensional variable $\boldsymbol{l}$, centered at $\mathbf{r}_0$ and covering the exposed substrate region Ω. This yields a time-dependent realization of the empirical field that satisfies the aforementioned SDE over ensemble averages:

$$\hat{n}(\mathbf{r}) \approx \frac{1}{\mathrm{d}\Omega}\sum_i \int_{\mathrm{d}\Omega} \mathrm{d}\boldsymbol{l}\,\delta(\mathbf{r}_i - \mathbf{r} + \boldsymbol{l}). \tag{12}$$

This Langevin formulation, which generates the empirical adatom density field, must also incorporate microscopic nucleation processes that lead to QD formation during heteroepitaxy. To account for this, we define the local nucleation free energy $G(\hat{n}, \mathbf{r}_0)$ as the free energy cost to assemble a cluster of $\hat{n}$ adatoms within a grid cell of width $\sqrt{d\Omega}$, centered at $\mathbf{r}_0$. This nucleation barrier is computed by evaluating the system energy $U_{\mathrm{sys}}[\hat{n}(\mathbf{r}, t)]$ on a constrained configuration in which $\hat{n}$ adatoms are localized near $\mathbf{r}_0$ and subtracting the reference energy of the homogeneous background state $\hat{n}(\mathbf{r}, 0) \approx 1/\Omega$:

$$G(\hat{n}, \mathbf{r}_0) = U_{\mathrm{sys}}[\hat{n}(\mathbf{r}_0, t)] - U_{\mathrm{sys}}[\hat{n}(\mathbf{r}_0, 0)]. \tag{13}$$

The function $G(\hat{n}, \mathbf{r}_0)$ captures the energetic tradeoff between interadatom interactions, strain relaxation, and the influence of boundary fields near $\mathbf{r}_0$. We denote the energy $U_{\mathrm{sys}}[\hat{n}(\mathbf{r}_0, t)]$ as the free energy, since the entropic contribution (compared with the strain and surface energies) is negligible under typical growth conditions [45].

The apparent complexity of the aforementioned free energy functional can be simplified within the coherent SK growth mode by adopting a classical LaMer nucleation model [51,52], which captures the essential competing mechanisms during coherent QD growth, where QDs are considered dislocation-free and exhibit symmetric shapes. Since the QD volume is directly proportional to the number of adatoms $\hat{n}$, for QD formation at a site $\mathbf{r}_0$ with an approximate nucleus diameter $d_{\mathrm{QD}} \approx \hat{n}^{1/3}$, the following model describes the competition between elastic strain energy relief and surface free energy, with magnitudes $\mathcal{E}_{\mathrm{el}}$ and γ_{surf}, respectively:

$$\Delta G_{\mathrm{LaMer}}(d_{\mathrm{QD}}) = -\epsilon_0^2 \mathcal{E}_{\mathrm{el}}[d_{\mathrm{QD}}]^3 + \gamma_{\mathrm{surf}}[d_{\mathrm{QD}}]^2, \tag{14}$$

where $\epsilon_0 = (a_{\mathrm{film}} - a_{\mathrm{sub}})/a_{\mathrm{sub}}$ is the lattice mismatch between the film (a_{film}) and the substrate (a_{sub}) lattice constants. The first term corresponds to the elastic strain energy relief with respect to the wetting layer, while the second term captures the energetic penalty for generating QD surfaces [52]. Motivated by the experimental observation of self-limited QDs [43], we introduce a phenomenological free energy term, $\Delta G_{\text{self-limited}} > 0$, which limits coherent QD growth and accounts for the emergence of a second local minimum in the free energy landscape:

$$\Delta G(d_{\mathrm{QD}}, \mathbf{r}_0) \approx \Delta G_{\mathrm{LaMer}}(d_{\mathrm{QD}}, \mathbf{r}_0) + \Delta G_{\text{self-limited}}(d_{\mathrm{QD}}, \mathbf{r}_0). \tag{15}$$

While attempts have been made to obtain the approximated form of this term [53], the exact mechanisms underlying self-limited QD sizes remain under debate (e.g., the competition between kinetic and thermodynamic processes) and are beyond the scope of this work [54,55]. Nevertheless, regardless of the detailed form of this free energy term, its existence, along with the engineered boundary field, plays a crucial role in manipulating the empirical density field of subsequently deposited adatoms, enabling semideterministic QD placement on the bulk surface.

As illustrated in Fig. 2, we present four regimes of the free energy ΔG that capture essential aspects of QD formation.

(1) Regime A (kinetic-driven seeding). Adatoms are continuously deposited on the bulk surface, where they stochastically migrate and contribute to the formation of surface layers on top of the substrate. On approaching the critical thickness, adatoms form temporary seeding clusters with subcritical density $\hat{n}_{\mathrm{seed}}$ as the starting seeds of QD growth.

(2) Regime B (seeding stabilization). On reaching the subcritical bulk volume, further adatom deposition leads to the formation of transient seeding clusters that are energetically favorable. These clusters may increase in local density $\hat{n}$ as they grow elastically. However, they remain susceptible to dissolution through thermal fluctuations or Ostwald ripening, in which smaller clusters are absorbed by larger ones to reduce the system's total surface energy, until they eventually exceed a supercritical density $\hat{n}_{\mathrm{supercritical}}$ [54].

(3) Regime C (coherent QD growth). Once clusters exceed the supercritical size, they grow continuously until a self-limited density $\hat{n}_{\text{self-limited}}$ is reached, at which point they become stable QDs. We note that the lattice mismatch must be sufficiently large to support stable QDs [45]. Although the stabilization mechanisms are still in debate, the second minimum of the free energy, $\Delta G_{\mathrm{LaMer}} + \Delta G_{\text{self-limited}}$, accounts for the existence of self-limited QDs. In contrast, the classical LaMer nucleation model, $\Delta G_{\mathrm{LaMer}}$, predicts unbounded QD growth corresponding to a global minimum. Nevertheless, both the existence of self-limited QDs and their influence on adatoms and neighboring QDs have been investigated extensively, both theoretically and experimentally.

(4) Regime D (self-limited QD formation). QDs reach a stationary size, and the addition of further adatoms is no longer energetically favorable (i.e., the QDs become metastable toward plastic growth), generating an effective repulsive force on nearby adatoms [55]. These QDs

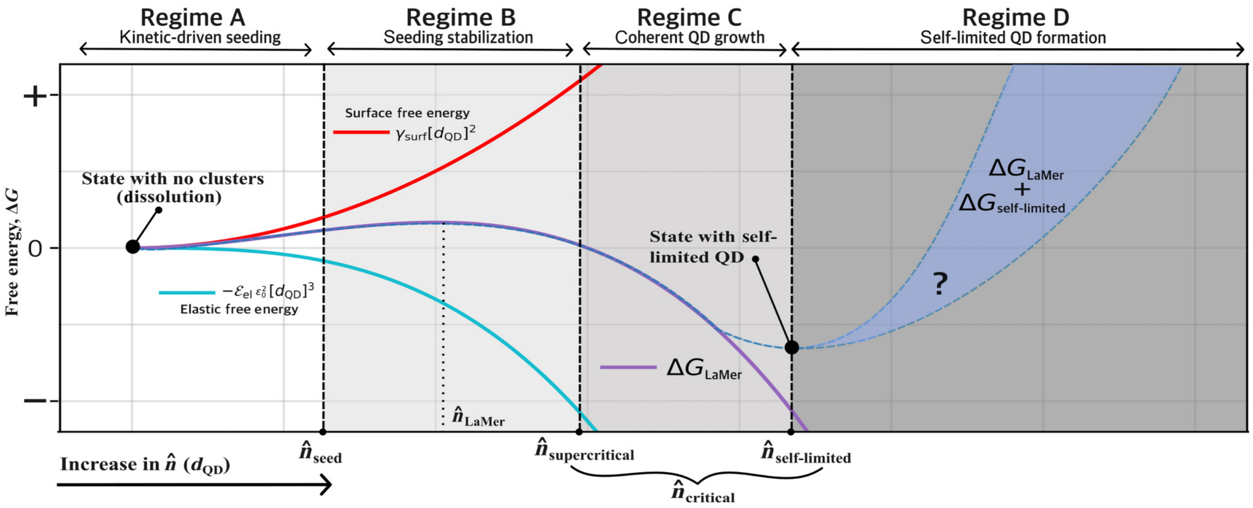

FIG. 2. Free energy landscapes with four regimes (shaded in different colors) of quantum dot (QD) formation, detailed in the main text. The formation of self-limited QDs exhibits two local minima, representing a dissolved state and a self-limited QD state, separated by a free energy barrier, peaking (local maximum) at the density $\hat{n}_{\mathrm{LaMer}}$. As defined in Eq. (14), the LaMer free energy $\Delta G_{\mathrm{LaMer}}$ (purple curve) represents, as a function of cluster density $\hat{n}$, the balance between the free energy contributions from interfacial elasticity (cyan curve) and the formation of the cluster surface (red curve). Four regimes (A–D) are separated by three characteristic densities, namely, subcritical density $\hat{n}_{\mathrm{seed}}$, supercritical density $\hat{n}_{\mathrm{supercritical}}$, and self-limited density $\hat{n}_{\text{self-limited}}$, associated, respectively, with the formation of temporary clusters, clusters leading to coherent QD growth, and self-limited (stable) QDs. In regime D (shaded in blue), the net free energy ΔG given in Eq. (15) may exhibit a convex behavior around the self-limited (stable) QDs; $\hat{n}_{\mathrm{supercritical}}$ and $\hat{n}_{\text{self-limited}}$ are referred to as a single critical density $\hat{n}_{\mathrm{crit}}$.

act as sources of strain fields that elastically distort the wetting layer and substrate [56]. As a consequence, a uniform spatial distribution of QDs emerges, as observed both experimentally and theoretically through kinetic Monte Carlo simulations [57,58].

While obtaining all microscopic parameters associated with these four regimes is challenging, we can obtain valuable insights on how to manipulate QDs by considering the following simplifications together with the aforementioned Langevin dynamics [Eq. (11)]. The aforementioned four regimes can be formalized through a time-dependent nucleation potential centered at $\mathbf{r}_0$, evolving as

$$V_{\mathrm{nc}}(\mathbf{r}-\mathbf{r}_0,t) = \begin{cases} V_{\mathrm{seed}}(\mathbf{r}-\mathbf{r}_0,t), & \text{if } |t-t_0| \le \tau, \\ V_{\mathrm{QD}}(\mathbf{r}-\mathbf{r}_0), & \text{if } \hat{n}(\mathbf{r}_0,t) \ge \hat{n}_{\text{self-limited}}, \\ 0, & \text{otherwise (dissolution).} \end{cases} \tag{16}$$

To model regimes A and B, we introduce a localized seed potential V_{seed} at $\mathbf{r}_0$ whenever the empirical density exceeds a subcritical threshold $\hat{n}_{\mathrm{seed}}$. The seeding potential serves as a binding potential V_{seed} that anchors nearby adatoms, promoting local adatom accumulation and cluster formation.

We model V_{seed} as a radially symmetric trapping potential with sufficient depth (relative to thermal fluctuations); the effective area of this potential is taken to be the underlying Monte Carlo grid size $d\Omega$. This seed persists for a finite duration τ_c, during which the local seed is allowed to either evolve toward the QD self-limited size with density $\hat{n}_{\text{self-limited}}$ at $\mathbf{r}_0$, corresponding to the second minimum in ΔG, or dissolve back to the uniform state (no clusters). The seed lifetime τ is drawn from an exponential distribution, $\tau \approx \exp(1/\tau_c)$, and t_0 denotes the first-passage time for seeding, defined as

$$t_0 = \min\left\{ t \,\middle|\, \hat{n}(\mathbf{r}_0,t) \ge \hat{n}_{\mathrm{seed}} \right\}. \tag{17}$$

If no QD nucleation occurs within the interval $[t_0, t_0+\tau]$, the seed potential is removed, corresponding to dissolution. Both the subcritical threshold $\hat{n}_{\mathrm{seed}}$ and supercritical density $\hat{n}_{\mathrm{supercritical}}$ are determined by detailed growth conditions. Since reaching the supercritical density $\hat{n}_{\mathrm{supercritical}}$ triggers coherent QD growth toward the self-limited density $\hat{n}_{\text{self-limited}}$, for computational simplicity, we merge these two points into a single reference and denote it as the critical density $\hat{n}_{\mathrm{crit}}$ (see Fig. 2). The supercritical and critical densities are taken to be of the same order of magnitude as the homogeneous background state; $\hat{n}_{\mathrm{crit}} \approx 10^3 \hat{n}_{\mathrm{seed}}$ and $\hat{n}_{\mathrm{seed}} \approx 10^2 \hat{n}(\mathbf{r}_0, 0)$.

As the empirical density reaches $\hat{n}_{\mathrm{crit}}$ within the time window τ_c, the seed potential is irreversibly converted to a stable QD potential V_{QD}, indicating successful traversal of the nucleation barrier into regime C, creating a permanent QD at $\mathbf{r}_0$, where it subsequently generates repulsion

(V_{QD}) to newly deposited adatoms, reflecting the stabilization of the dot and the inhibition of further growth beyond the self-limited size.

The detailed interatomic interactions among adatoms, between adatoms and QDs, and among QDs depend on the growth conditions and specific atomic properties, such as bond ionicity and van der Waals interactions, and are typically obtained from empirical studies [43]. For the purpose of demonstrating semideterministic QD placement, we model the pairwise repulsion between adatoms (dipole-dipole) and between adatoms and QDs (dipole-monopole) [59], denoted V_{nc}, using a generic screened Coulomb-like potential V, expressed as

$$V\big(\mathbf{r}-\mathbf{r}'\big) \approx \frac{\exp\left[-\xi \left|\boldsymbol{\ell}^{-1}(\mathbf{r}-\mathbf{r}')\right|\right]}{\left|\boldsymbol{\ell}^{-1}(\mathbf{r}-\mathbf{r}')\right|^{\alpha}}. \tag{18}$$

Here, ξ is a screening parameter that sets the scale and the characteristic decay length-scale tensor is defined as $\boldsymbol{\ell} = \sqrt{\mathbf{D}/\lambda}$, where λ is the constant desorption rate that sets the interaction scale. The power-law exponent α is a microscopic parameter that characterizes the type and range of the many-body interactions. For example, a dipole-monopole interaction corresponds to $\alpha = 2$, while a dipole-dipole interaction corresponds to $\alpha = 3$.

The system energy is updated by incorporating the time-dependent nucleation potential

$$U_{\mathrm{sys}} \to U_{\mathrm{sys}} + \frac{1}{2}\iint_{\Omega} \hat{n}(\mathbf{r},t)\, V_{\mathrm{nc}}(\mathbf{r}-\mathbf{r}_0,t)\, \hat{n}(\mathbf{r}_0,t)\, d\mathbf{r}\, d\mathbf{r}_0, \tag{19}$$

and the Langevin dynamics are modified accordingly. The pairwise interaction w in U_{sys} [Eq. (8)] is approximated as a point-like elastic dipole interaction at long range and is assumed to be repulsive. This discourages adatoms from clustering too soon, favors nucleation at distinct sites, and contributes to the size uniformity of QDs [43,59].

The boundary field is modeled as a delta-function sink potential, modulated by the (dimensionless) local strain profile $\sigma[\mathbf{r}_{\mathrm{bd}}(u)]$, which prevents adatoms from escaping once they reach the boundary:

$$B\left[\mathbf{r}-\mathbf{r}_{\mathrm{bd}}(u)\right] = -B_0\, \sigma[\mathbf{r}_{\mathrm{bd}}(u)]\, \delta\left[\mathbf{r}-\mathbf{r}_{\mathrm{bd}}(u)\right]. \tag{20}$$

This formulation allows adatoms to migrate tangentially along the boundary. The sign of the strain profile σ encodes the local stress state: compressive strain (positive σ) attracts adatoms, while tensile strain (negative σ) repels them. While, in general, the boundary field strength would vary, owing to inhomogeneity along the boundary profile, we assume that the strain results from local lattice mismatch and thus depends only on the local boundary curvature.

IV. LINEAR PERTURBATION THEORY IN THE DILUTED LIMIT

In the early stage of heteroepitaxy, thermally driven stochastic migration of adatoms causes preferential deposition at boundary edges orthogonal to the fast diffusion axis $\hat{\mathbf{x}} \equiv [1\bar{1}0]$ [27], followed by lateral spreading along the boundary, as shown numerically in Fig. 3(c). When the average empirical density $\hat{n}$ over the exposed region Ω remains much smaller than the homogeneous density limit, the adatom dynamics are primarily governed by anisotropic diffusion. We refer to this regime as the "diluted limit," where the exposed region Ω remains effectively adatom-free.

It is important to note that, locally, the empirical density may exceed this limit on the boundary. Depending on the repulsion strength between adatoms and the critical seeding density, such local accumulation can initiate the early stages of quantum dot nucleation.

We coarse-grain the empirical field $\hat{n}$ into a continuous density field n, and introduce a decay term to account for the finite lifetime of adatoms, characterized by a constant desorption rate λ. Expanding locally around a boundary point $\mathbf{r}_{0,\mathrm{bd}} = (x_0, y_0)$, we assume that the convection-reaction-diffusion dynamics are separable to linear order along the principal axes. This yields a local density field n_0, modulated by separable spatial factors $f(x-x_0)$ and $g(y-y_0)$, such that

$$\begin{aligned} n(\mathbf{r}_{\mathrm{bd}}) &= f\,(x-x_0)\cdot g(y-y_0)\cdot n_0 \\ &\Rightarrow \ln n = \ln f + \ln g + \ln n_0. \end{aligned} \tag{21}$$

Near the boundary point $\mathbf{r}_{0,\mathrm{bd}}$, the change in current density along the boundary curve is given by

$$\frac{d\mathbf{J}}{ds}(\mathbf{r}_{\mathrm{bd}}) = \frac{dJ_{\parallel}}{ds}\,\hat{\mathbf{T}} + J_{\parallel}\,\frac{d\hat{\mathbf{T}}}{ds} = \frac{dJ_{\parallel}}{ds}\,\hat{\mathbf{T}} + \kappa J_{\parallel}\,\hat{\mathbf{N}}, \tag{22}$$

where $\kappa(\mathbf{r}_{0,\mathrm{bd}})$ is the local curvature, describing how rapidly the boundary turns at $\mathbf{r}_{0,\mathrm{bd}}$. The vectors $\hat{\mathbf{T}}$ and $\hat{\mathbf{N}}$ are the local tangent and outward normal vectors, respectively, evaluated at the boundary.

The tangential component of the current density is defined as

$$J_{\parallel}\left(\mathbf{r}_{\mathrm{bd}}-\mathbf{r}_{0,\mathrm{bd}}\right) = -\hat{\mathbf{T}}\cdot\mathbf{D}\nabla n, \qquad \kappa\left(\mathbf{r}_{0,\mathrm{bd}}\right)\cdot\hat{\mathbf{T}}\cdot\mathbf{D}\nabla n \geq 0, \tag{23}$$

and, for consistency, we adopt the convention that the adatom flow aligns with the direction in which the boundary turns. This convention does not affect the physical direction of adatom motion but serves to interpret the sign of the local current density magnitude. Positive values correspond to accumulation, while negative values indicate depletion, with the sign further modulated by the local strain profile.

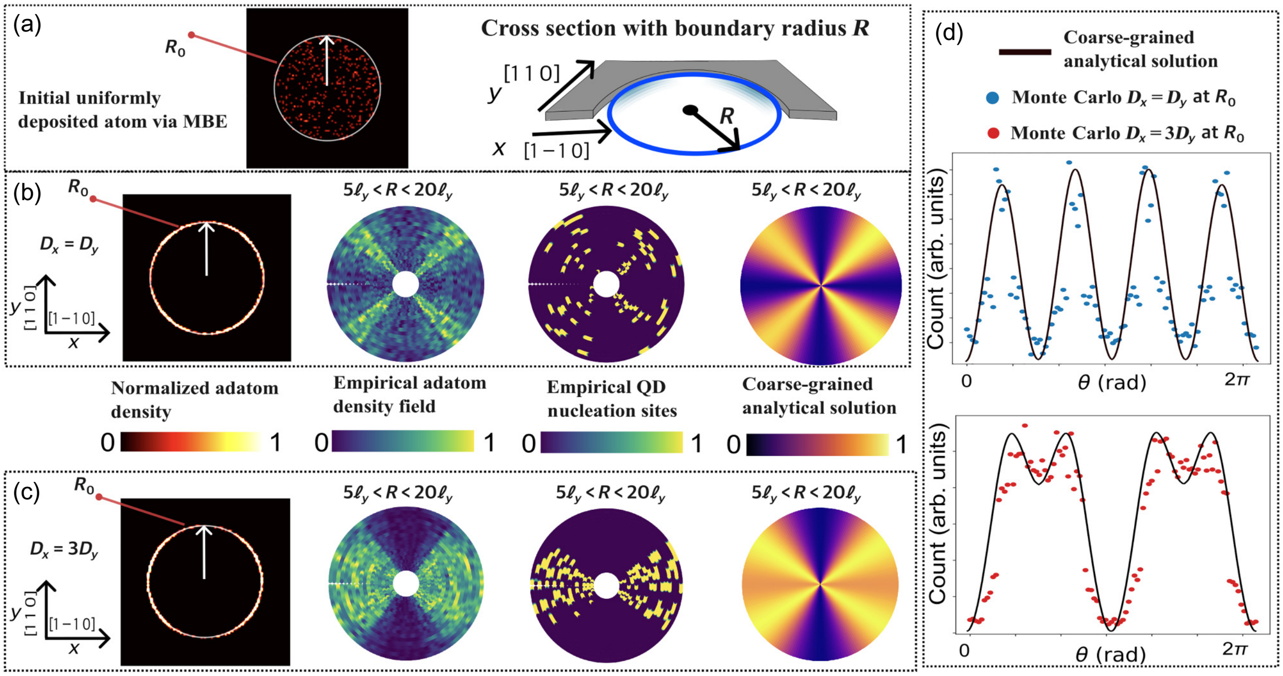

FIG. 3. Detailed comparison of empirical adatom density field (Monte Carlo sampled), quantum dot (QD) nucleation, and mean-field analytical adatom density field solutions under a homogeneous circular boundary field, for both isotropic diffusion ($D_x = D_y$) and anisotropic diffusion ($D_x = 3D_y$) along the boundary. (a) Atomic flux is uniformly deposited from an epitaxy source onto the center of a circular patterned substrate with radius $R_0 = 10\,\ell_y$, where ℓ_y is the diffusion length in the $\hat{\mathbf{y}}$ direction. MBE, molecular beam epitaxy. (b, c) The first (leftmost) column shows the empirical adatom density field at a given radius $R_0 = 10\,\ell_y$. Owing to diffusion, adatoms accumulate at the boundary, and the resulting spatial distribution depends on the diffusion anisotropy. For isotropic diffusion, the empirical density exhibits radial symmetry, while for anisotropic diffusion, the distribution becomes directionally biased. The second column shows radial statistics extracted from various radii with respect to the diffusion length $5\,\ell_y < R < 20\,\ell_y$, further illustrating the breakdown of axial symmetry under anisotropy. In both columns, pairwise interactions are turned off ($w = 0$) and the nucleation potential is absent ($V_{\text{nc}} = 0$). The third column incorporates a nonzero nucleation potential ($V_{\text{nc}} \neq 0$) and displays the resulting QD nucleation sites for various radii, $5\,\ell_y < R < 20\,\ell_y$. Nucleation events are strongly correlated with regions of high adatom density. The fourth column presents mean-field analytical solutions obtained from Eq. (30). (d) Cross section comparison between mean-field analytical solutions and Langevin-based Monte Carlo simulations at a given radius $R_0 = 10\,\ell_y$, evaluated with respect to angular parametrization under both isotropic and anisotropic conditions.

The local continuity equation at the boundary point $\mathbf{r}_{0,\text{bd}}$ is given by

$$\partial_t n = -\hat{\mathbf{T}} \cdot \nabla J_\parallel - \kappa\, \text{Sign}\left[\sigma\left(\mathbf{r}_{0,\text{bd}}\right)\right] J_\parallel - \lambda n, \tag{24}$$

where the sign of the local strain profile, $\text{Sign}[\sigma(\mathbf{r}_{0,\text{bd}})]$, determines the nature of the curvature-driven contribution: compressive strain ($\text{Sign} = +1$) promotes adatom accumulation over time, while tensile strain ($\text{Sign} = -1$) drives depletion.

Substituting the expression for $J_\parallel$ into Eq. (24), we have

$$\hat{\mathbf{T}} \cdot \nabla \left(\hat{\mathbf{T}} \cdot \mathbf{D}\nabla n\right) + \text{Sign}[\sigma(\mathbf{r}_{0,\text{bd}})]\,\kappa \left(\hat{\mathbf{T}} \cdot \mathbf{D}\nabla n\right) - \lambda n = 0, \tag{25}$$

which can be separated into a system of two PDEs, for $f\,(x - x_0)$ and $g(y - y_0)$, respectively.

Expanded in Cartesian components around the boundary point $\mathbf{r}_{0,\text{bd}}$, the local convection-diffusion-reaction equations take the form

$$\begin{aligned} \frac{\partial f}{\partial t} &= T_x^2 D_x \frac{\partial^2 f}{\partial x^2} + \kappa\, T_x D_x \frac{\partial f}{\partial x} - \lambda f\,, \\ \frac{\partial g}{\partial t} &= T_y^2 D_y \frac{\partial^2 g}{\partial y^2} + \kappa\, T_y D_y \frac{\partial g}{\partial y} - \lambda g, \end{aligned} \tag{26}$$

where $T_x = \hat{\mathbf{T}} \cdot \hat{\mathbf{x}}$ and $T_y = \hat{\mathbf{T}} \cdot \hat{\mathbf{y}}$ denote the projections of the local tangent direction along the two principal diffusion axes. These equations are invariant under parity transformation ($x \to -x, y \to -y$).

The first-order expansion near a boundary point elucidates the interplay between anisotropic diffusion and geometric modulation, yielding a tractable expression for the stationary adatom density profile along and near the boundary. The general steady-state solution of the adatom density field can be constructed as a product of first-order expansions using the boundary parametrization u, where θ is the corresponding angular variable:

$$\frac{n(u_N)}{n_0} = \prod_{i=0}^{N} \sum_{c,c'=\pm 1} A^i_{c,c'} e^{\left[du_i\left(k_x^c|T_x(u_i)|+k_y^{c'}|T_y(u_i)|\right)\right]}, \qquad (27)$$

where $A^i_{c,c'}$ is a coefficient determined by boundary conditions and local geometry, and du_i denotes the local boundary segment at u_i. Recalling that $\mathbf{r}_{\rm bd}(u)$ is a unit-speed trajectory ($|d\mathbf{r}_{\rm bd}(u)/du| = 1$), we have

$$\frac{dv_i}{du_i} = |T_v(u_i)| \approx \frac{|v(\theta_{i+1}) - v(\theta_i)|}{du_i}, \qquad v = x, y, \quad (28)$$

where $v = x, y$ labels the primary diffusion axes. The exponent in Eq. (27) can be compactly written as (Appendix A)

$$k_v^c|T_v(u_i)| = \frac{\kappa(u_i)}{2} + c\,\mathcal{K}_v(u_i),$$

$$\ell_v = \sqrt{\frac{D_v}{\lambda}}, \qquad \mathcal{K}_v(u_i) = \sqrt{\left[\frac{\kappa(u_i)}{4}\right]^2 + \ell_v^{-2}}, \qquad (29)$$

where D_x and D_y are the diagonal elements of the diffusion tensor $\mathbf{D}$ and ℓ_x, ℓ_y define the characteristic decay lengths along the two principal diffusion axes.

In the continuum limit, the general steady-state solution assumes a path-integral form,

$$\frac{n(u)}{n_0} = \int \mathcal{D}[\mathbf{c}, \mathbf{c}'] \exp\left[\int_0^u d\tilde{u}\Big(\kappa(\tilde{u}) + \mathbf{c}(\tilde{u})\,\mathcal{K}_x(\tilde{u}) + \mathbf{c}'(\tilde{u})\,\mathcal{K}_y(\tilde{u})\Big)\right], \qquad (30)$$

where the functional integral $\int \mathcal{D}[\mathbf{c}, \mathbf{c}']$ represents the sum over all possible sign trajectories for $(\mathbf{c}, \mathbf{c}')$,

$$\int \mathcal{D}[\mathbf{c}, \mathbf{c}'] \ldots = \iint \mathcal{D}[\mathbf{c}]\,\mathcal{D}[\mathbf{c}']\,A[\mathbf{c}, \mathbf{c}'] \ldots \qquad (31)$$

We compare the analytical steady-state adatom density field given in Eq. (30), under the mean-field approximation detailed in Appendix B, for both the biaxial diffusion–dominated condition (i.e., circles with constant curvature) and the curvature-dominated condition (i.e., ellipses with variable curvature). To model the adatom density on the boundary, atoms are initially deposited uniformly within a fixed geometry to mimic the initial epitaxial conditions. The boundary field B acts as a sink potential: once adatoms reach the boundary, they migrate only along it via projected Langevin dynamics, in contrast to the full 2D Langevin dynamics that govern motion in the bulk.

In Figs. 3, 4, and 5, using Eq. (16), we systematically investigate QD nucleation profiles in the diluted limit across various boundary geometries, where stochastic seeding events occur almost exclusively at the boundary. The seeding probability is modulated by the adatom density field, which reflects the combined influences of biaxial diffusion, boundary field effects, and curvature. In the simulations, the ensemble-averaged empirical adatom density field $\langle \hat{n} \rangle$ is obtained from Langevin-based Monte Carlo sampling.

As shown in Fig. 3, this comparison is performed across multiple concentric circular boundaries of varying radii, under both isotropic and anisotropic diffusion conditions [Figs. 3(b) and 3(c)]. When the QD nucleation potential $V_{\rm nc}$ is included, QDs are distributed along the boundary, with spatial profiles that closely resemble the empirical adatom density fields. The spacing between boundary QDs is determined by the interplay of diffusion, geometry, and $V_{\rm nc}$. For instance, once a QD nucleates at a given location along the boundary, it increases the local chemical potential, generating effective repulsive interactions that redirect subsequent adatoms to other regions.

In Fig. 3(d), we construct the analytical solutions of the coarse-grained model under the mean-field approximation and compare them with empirical adatom density results, demonstrating quantitative agreement in capturing the stationary spatial features.

In both isotropic and anisotropic cases, peaks in the adatom density field correspond to regions of enhanced seeding probability, where adatoms are more likely to form temporary clusters. These clusters represent the initial stage of QD formation. Once temporary clusters form in regions of high density, the seeding potential $V_{\rm seed}$ attracts additional adatoms deposited during heteroepitaxy, leading to the formation of stable QDs along the boundary.

To further quantify the contribution of curvature to the adatom density field along the boundary beyond the case of uniform curvature, we extend the previous formulation to elliptical boundary geometries (Appendix C), as shown in Fig. 4(a). In Figs. 4(b) and 4(c), we construct analytical solutions of the coarse-grained model under the mean-field approximation for different axial orientations under both isotropic and anisotropic diffusion, and compare them with the corresponding empirical density fields obtained from Langevin-based Monte Carlo simulations. In regions where the empirical adatom density becomes locally elevated, QD seeding events become statistically favorable. This effect, combined with the fact that regions of high curvature act as effective traps for adatoms, suggests that both biaxial diffusion and local curvature can serve as tuning parameters to control adatom density fields and thus QD nucleation sites along boundary contours. Since boundary geometries can be arbitrarily fabricated, as illustrated in

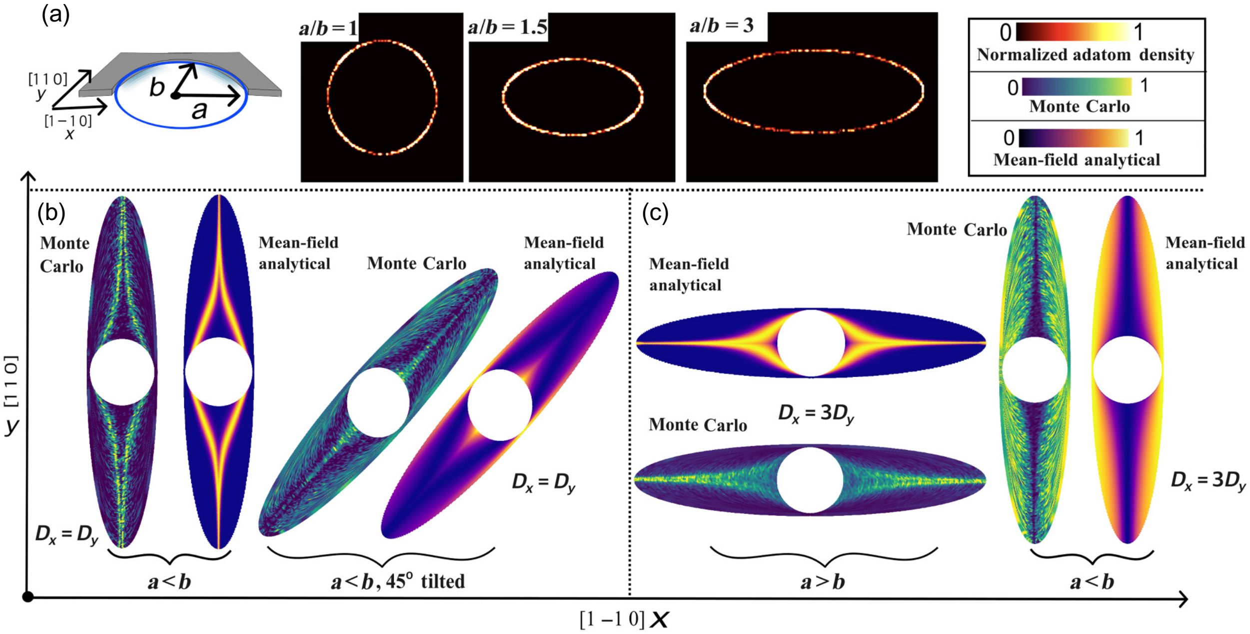

FIG. 4. Detailed comparison between empirical adatom density fields (Monte Carlo) and mean-field analytical adatom density field solutions under a homogeneous elliptical boundary field for isotropic diffusion ($D_x = D_y$) and anisotropic diffusion ($D_x = 3D_y$) along the boundary. (a) Elliptical boundaries with varying aspect ratios and the corresponding empirical adatom density fields. (b, c) Radial statistics extracted from ellipses with different aspect ratios under isotropic diffusion ($D_x = D_y$) and anisotropic diffusion ($D_x = 3D_y$), respectively. The semimajor axis a is oriented parallel ($a > b$), at a 45° tilt ($a < b$), and orthogonal ($a < b$) to one of the diffusion axes $\hat{\mathbf{x}}$. By incorporating local curvature contributions, the resulting mean-field analytical solutions reproduce key features observed in the Monte Carlo–sampled empirical density fields.

Fig. 5, this approach enables flexible design strategies for device applications.

As the total number of deposited atoms increases, repulsive pairwise interactions w [see Eq. (18)] become non-negligible. This results in a modification of the steady-state solution, $n_{\text{int}}(x,y) \approx n(x,y)\exp[q(w)]$, where $q(w)$ is a functional of the interaction strength that broadens the density field along the boundary contour. Intuitively, as repulsive interactions increase, adatoms tend to avoid regions of high density, resulting in a smeared-out density profile along the boundary, as shown in Fig. 5(a). The governing PDE in Eq. (25) thus becomes coupled through the pairwise interaction term, and nontrivial spatial correlations arising from local curvature and boundary nucleation potentials must be taken into account.

As additional adatoms are deposited, they become “aware” of the surrounding strain field, generated by both the engineered boundary and primary QDs nucleated at high-curvature boundary regions. This evolving strain landscape dynamically alters subsequent QD nucleation sites at the boundaries and within the bulk (pristine surface). Building on this, in the following section, we utilize strain sensitivity, together with engineered boundary fields, to guide QD nucleation in a controlled manner, enabling semideterministic QD placement.

V. SECONDARY QD FORMATION ON PRISTINE SURFACE

A stable InAs/GaAs QD on a pristine surface has a typical size range of 20 to 25 nm, with nucleation sites that are both highly sensitive to material properties and growth conditions. The interaction length scale of the nucleation potential V_{nc} can extend to several tens of nanometers, or even up to hundreds of nanometers, as inferred from the observed relationship between QD density and growth rate, or QD array periodicity [60,61]. In contrast, stable QDs formed at the boundary often exhibit irregular shapes and accumulated stress profiles, which can result in comparable or even greater interaction length scales, ranging from a few nanometers to several hundred nanometers. The repulsive field generated by those stable QDs at the boundary not only affects the migration of nearby adatoms but also interacts with adatom densities in the bulk (pristine surface), influencing the global spatial accumulation and redistribution of newly deposited adatoms, which can be used to statistically control the seeding location on the pristine bulk surface. This concept is illustrated schematically in Fig. 6.

As demonstrated in Fig. 7, to model boundary-mediated secondary QD nucleation, we begin with an elongated

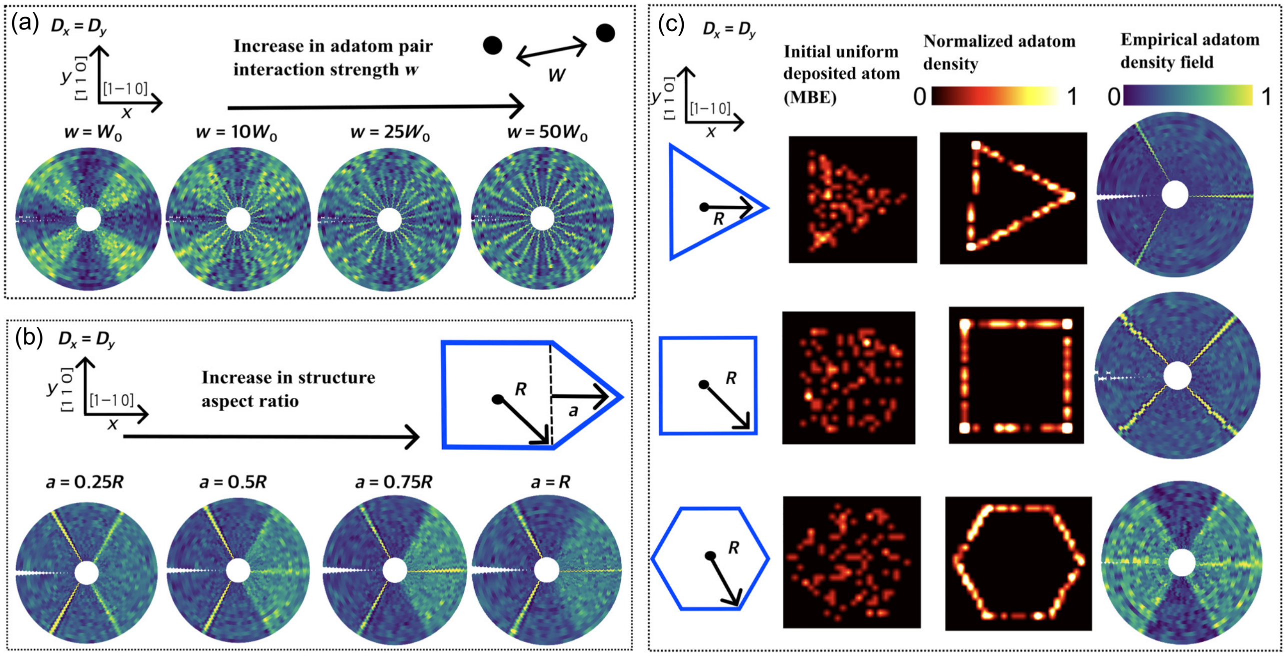

FIG. 5. Geometric tuning of empirical adatom density fields under isotropic diffusion ($D_x = D_y$). (a) By incorporating a nonzero repulsive pairwise interaction potential w between adatoms, the resulting empirical adatom density field exhibits a smeared-out asymptotic density profile along the boundary contour. (b) Starting from a lozenge boundary, elongation of the right-side flat edge with an aspect ratio a/R induces local anisotropic confinement, leading to enhanced adatom accumulation near the elongated region. This demonstrates that local curvature can modulate the spatial profile of the adatom density field along the boundary. (c) Simulations with various boundary geometries under initially uniform atomic deposition illustrate the flexibility and adaptability of the modeling framework in capturing geometry-tunable adatom density profiles and quantum dot nucleation behavior along the boundary contour. MBE, molecular beam epitaxy.

lozenge boundary field design and vary the right-side diagonal coordinate $(a, 0)$ from $-0.6L$ to $2L$, while conserving the total bulk area. The epitaxial deposition of new atoms is introduced sequentially at a rate much slower than the time required for adatoms to reach a steady-state distribution through Langevin dynamics. We then record the spatial distribution corresponding to the *first* QD nucleation site, as illustrated on the far right side of Fig. 6(e). This process is repeated 400 times using different initial random adatom configurations (uniformly distributed). Depending on the value of a, as shown in Fig. 7(b) and Fig. 8 in Appendix D, the resulting spatial distribution of stable QDs exhibits a boundary-dependent profile. The observed inhomogeneity in the QD distribution reveals statistically preferential nucleation sites. As detailed in Fig. 9 in Appendix D, we further perform a full parameter sweep over $a \in [-0.6L, 2L]$ for a hexagonal boundary field with 60° orientation. While the microscopic parameters of the Langevin dynamics remain unchanged, the hexagonal boundary field produces a more spatially extended adatom density field, compared with the elongated lozenge boundary field shown in Fig. 8 in Appendix D.

Intuitively, semideterministic placement is expected: on achieving primary QD distribution along the engineered boundary field, subsequent adatoms mainly diffuse along the fast axis (and scarcely along the slow axis) and experience secondary interactions that can be significantly slowed down when near primary QDs, leading to adatom accumulation over time at those locations.

While the aforementioned simulation is conducted at mild anisotropy, $D_x = 3D_y$, for illustration purposes, in the case of the GaAs (001)-$\beta_2(2 \times 4)$ surface with diffusion axes $\hat{\mathbf{x}} \equiv [1\bar{1}0]$ and $\hat{\mathbf{y}} \equiv [110]$, the diffusion constant and anisotropy, $D_x \approx 10^3 D_y \approx 1 \times 10^{-3}$ $\mu\text{m}^2/\text{s}$ along the two directions, follow at typical temperatures $T \approx 500$ K [46], which gives the relative diffusion length scale $\ell_x/\ell_y \approx 32$. This suggests that an efficient redistribution of the empirical density field occurs along the fast diffusion axis. Therefore, we predict that, by engineering boundary fields with anisotropy along the fast diffusion axis (for example, shape edges across two opposite boundaries, see the comparison in Figs. 8 and 9 in Appendix D), the modulation effects from both the boundary fields and the on-boundary primary nucleated QDs would exert the strongest influence on subsequently deposited adatoms, leading to more pronounced modulation that enables semideterministic placement of secondary QDs.

Since we assume a quasistationary limit, the deposition rate must be sufficiently low to allow adatoms to reach quasiequilibrium. Let us consider a unit deposition

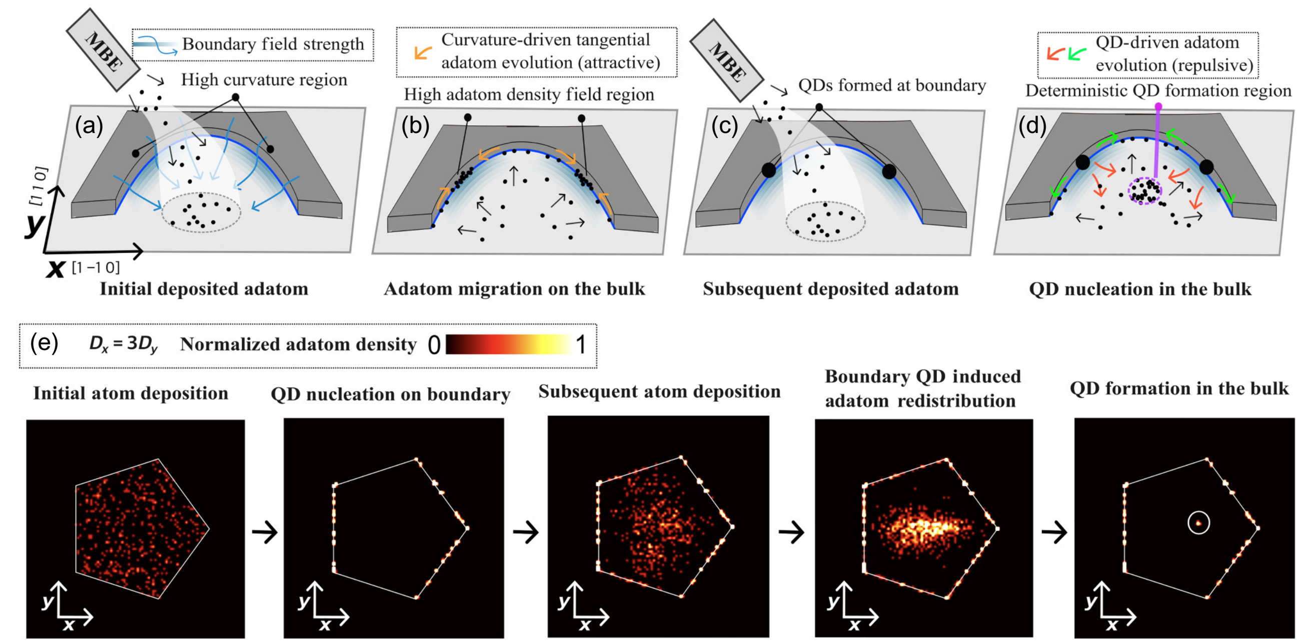

FIG. 6. Semideterministic quantum dot (QD) placement guided by a boundary-induced chemical potential landscape. MBE, molecular beam epitaxy. (a) Atoms are vertically deposited via an epitaxy source onto a patterned substrate with an embedded boundary field (field strength illustrated by the blue gradient), as defined in Fig. 1. (b) Anisotropic diffusion drives adatoms toward the boundary, where their motion becomes confined on arrival. As described in Eq. (25), adatoms preferentially cluster in regions of high positive curvature (e.g., concave segments with compressive strain), increasing the local empirical adatom density (black dots) and promoting QD nucleation at these locations. (c) Following initial QD formation at the boundary, additional atoms are vertically deposited via continued epitaxy at a much lower rate than the rate at which adatoms reach the steady state. (d) The presence of boundary QDs reshapes the local chemical potential landscape. Repulsive interactions from existing QDs redirect adatom migration either tangentially along the boundary (green arrows) or outward into the substrate interior (red arrows). These combined effects promote secondary QD nucleation within the bulk, enabling semideterministic and spatially reproducible QD patterning mediated by boundary-induced adatom dynamics. (e) Snapshots from Monte Carlo simulations where the pentagon boundary profile is used to illustrate each of the process steps described. Circles indicate stable QDs, while red dots represent adatoms.

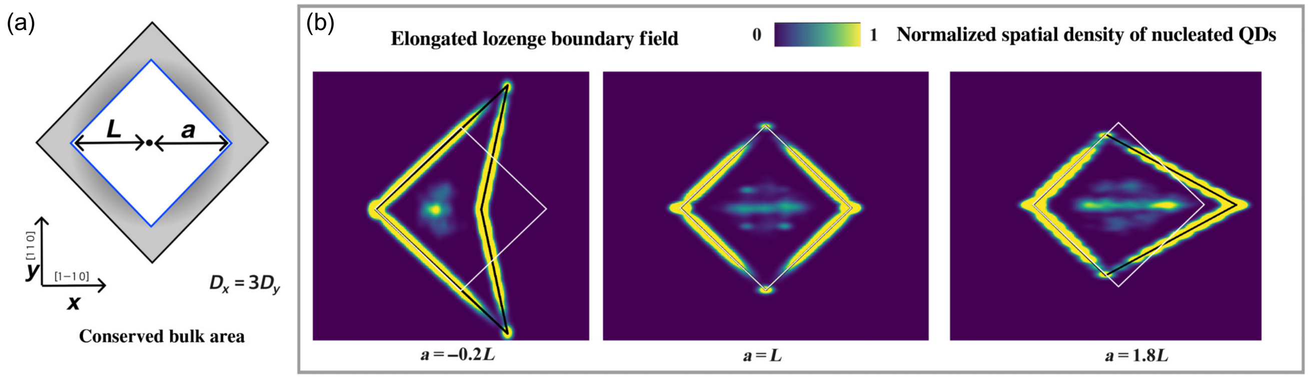

FIG. 7. Boundary-mediated semideterministic quantum dot (QD) placement via full-scale Langevin dynamics ($D_x = 3\,D_y$). (a) A lozenge domain with a tunable right-side diagonal coordinate $(a, 0)$, where $a \in (-0.6L, 2L)$, is used while keeping the total bulk area constant. (b) Spatial distribution of the first QD nucleation site within the bulk for different aspect ratios, sampled from statistics over 400 distinct random adatom initializations (i.e., independently of initial conditions). Although QDs nucleate stochastically, the resulting distribution exhibits statistically localized behavior that is tunable solely through boundary field design, demonstrating the principle of semideterministic QD placement. A detailed parameter sweep is provided in Fig. 8 in Appendix D. We note that these "QD distributions" are independently sampled statistics based on different initial adatom density profiles (i.e., they are not clusters of QDs), and they represent realizations that reflect the probability of possible QD nucleation sites.

time, with adatom diffusion lengths of $\ell_x \approx 32\,\mathrm{nm}$ and $\ell_y \approx 1\,\mathrm{nm}$. The effective diffusion area is then $d\Omega \approx \ell_x \cdot \ell_y = 32\,\mathrm{nm}^2$. The deposition flux F (atoms per unit area, per unit time) corresponding to N atoms deposited in this area is given by $F \approx N/d\Omega$. In the quasistationary limit, within unit time, the number of deposited adatoms over the effective area should be much smaller than one adatom per diffusion area. Taking the bound $N = 1$, the corresponding flux is $F = 1/(32\,\mathrm{nm}^2 \cdot 1\,\mathrm{s}) \approx 3.125 \times 10^4\,\mathrm{atoms}/(\mathrm{mm}^2\,\mathrm{s})$. To convert this to a deposition rate in monolayers per second (ML/s), we use the lattice constant of GaAs ($a = 0.565\,\mathrm{nm}$) to calculate the surface atomic density as $n_s = 2/a^2 \approx 6.26 \times 10^6\,\mathrm{atoms/mm}^2$. This gives the upper bound on the deposition rate $R_{\mathrm{bound}} = F/n_s \approx 5 \times 10^{-3}\,\mathrm{ML/s}$, which is consistent with typical growth rates used for InAs QDs on GaAs(001) substrates [62]. To achieve the quasistationary limit, the empirical deposition rate must satisfy $R \ll R_{\mathrm{bound}}$ around temperatures $T \approx 500$ K, which can be realized under experimental conditions.

Practically, designing such boundary fields is straightforward with standard fabrication capabilities. A typical hard mask can first be uniformly deposited across the substrate [e.g., a (001)-oriented GaAs surface], and then selectively etched to re-expose patterned regions for regrowth.

VI. DISCUSSION AND CONCLUSION

Over the past few decades, strain-mediated interactions between QDs and adatoms have been extensively studied theoretically, focusing on QD morphology and phase transitions, yet few studies have explored their use in practical applications, such as QD placements. In this work, we have theoretically and numerically investigated the interplay between geometry, diffusion, and stochastic dynamics in the context of quantum dot (QD) nucleation from empirical adatom density fields. Our results illustrate how geometric properties of boundary contours, such as curvature and orientation relative to anisotropic diffusion axes, along with intrinsic microscopic properties, such as adatom interactions and QD nucleation dynamics, shape the spatial patterns of QD formation.

In the early stage of epitaxy, referenced as the diluted limit, adatoms are preferentially accumulated along the boundary contour, where curvature enhances the local adatom density fields, which can be described by the path-integral formulation of a coarse-grained theory. As nucleated QDs accumulate on the boundary, their presence introduces a repulsive interaction field that dynamically alters the chemical potential landscape within the bulk. This feedback mechanism effectively shifts the nucleation zone away from the initial boundary, giving rise to secondary QD populations within the bulk, as demonstrated numerically via the fully scale Langevin dynamics simulations.

While this effect has not yet been experimentally realized, it has broad implications for nanofabrication strategies where precise spatial control of QDs is required in conjunction with complex device architectures. For example, on-chip indistinguishable multiphoton sources require simultaneous electrical tuning and coordination to dynamically bias individual QDs into their trion states; this is essential for constructing large-scale photonic cluster states, a key component of measurement-based quantum computing [63–66]. Furthermore, the controlled spatial arrangement of QDs enables systematic investigations of decoherence, dissipation, and entanglement propagation in open quantum systems [67,68], where spatial correlations and engineered environments play a central role [69,70].

This work enables the semideterministic positioning of high optical-quality self-assembled quantum dots on pristine surfaces, opening a new direction for next-generation on-chip photonic devices.

ACKNOWLEDGMENTS

We thank Chen Shang, Paul J. Simmonds, and John E. Bowers for their insightful discussions and suggestions. We acknowledge support from NSF Awards No. 2427169, No. 2137740, and No. Q-AMASE-i, through Grant No. DMR-1906325, and from NWO Quantum Software Consortium (Grant No. 024.003.037).

DATA AVAILABILITY

The data that support the findings of this article are openly available [71].

APPENDIX A: STEADY-STATE SOLUTIONS

We first assume $\kappa = 0$; as an example, the curvature-free steady-state solution in the x-direction is given by

$$\begin{aligned} T_x^2 D_x \frac{\partial^2 f}{\partial x^2} - \lambda f &= 0, \quad f(x) \approx e^{k_x^{\pm}|x-x_0|}, \\ T_x^2 D_x\,(k_x^{\pm})^2 - \lambda = 0 &\implies (k_x^{\pm})^2 = \frac{\lambda}{T_x^2 D_x}. \end{aligned} \tag{A1}$$

In general, the coefficients presented in Eq. (27) have the following form:

$$k_v^{\pm} = \frac{\kappa T_v D_v \pm \sqrt{(\kappa T_v D_v)^2 + 4T_v^2 D_v \lambda}}{2T_v^2 D_v}. \tag{A2}$$

APPENDIX B: PATH-INTEGRAL FORMULATION AND MEAN-FIELD APPROXIMATION

Starting from a reference point on the boundary, we can obtain a general solution for the coarse-grained adatom density field by considering the following:

$$\begin{aligned}\frac{n(\theta_N)}{n_0} &= \prod_{i=0}^{N} \sum_{c,c'=\pm 1} A^i_{c,c'} \exp\left(k^c_x|x(\theta_{i+1}) - x(\theta_i)| + k^{c'}_y|y(\theta_{i+1}) - y(\theta_i)|\right) \\ &= \prod_{i=0}^{N} \sum_{c,c'=\pm 1} A^i_{c,c'} \exp\left(du_i(k^c_x|T_x(u_i)| + k^{c'}_y|T_y(u_i)|)\right). \end{aligned} \tag{B1}$$

We further simplify Eq. B1 by noting that

$$k^c_x|T_x(u_i)| = \frac{\kappa}{2} + c\sqrt{\left(\frac{\kappa}{4}\right)^2 + \ell_x^{-2}}, \qquad k^{c'}_y|T_y(u_i)| = \frac{\kappa}{2} + c'\sqrt{\left(\frac{\kappa}{4}\right)^2 + \ell_y^{-2}}, \tag{B2}$$

where $\ell_x^{-1} = \sqrt{\lambda/D_x}$ and $\ell_y^{-1} = \sqrt{\lambda/D_y}$ represent the diffusion lengths along the x- and y-directions, respectively.

Substituting these expressions, we obtain

$$\begin{aligned}\frac{n(\theta_N)}{n_0} &= \prod_{i=0}^{N} \sum_{c_i,c_i'=\pm 1} A^i_{c_i,c_i'} \exp\left[du_i\left(\kappa(u_i) + c_i\sqrt{\left(\frac{\kappa(u_i)}{4}\right)^2 + \ell_x^{-2}} + c_i'\sqrt{\left(\frac{\kappa(u_i)}{4}\right)^2 + \ell_y^{-2}}\right)\right] \\ &= \sum_{\mathbf{c},\mathbf{c}'} A_{\mathbf{c},\mathbf{c}'} \prod_{i=0}^{N} \exp\left[du_i\left(\kappa(u_i) + \mathbf{c}_i\sqrt{\left(\frac{\kappa(u_i)}{4}\right)^2 + \ell_x^{-2}} + \mathbf{c}_i'\sqrt{\left(\frac{\kappa(u_i)}{4}\right)^2 + \ell_y^{-2}}\right)\right], \end{aligned} \tag{B3}$$

where $\mathbf{c} = [1, -1, 1, 1, \ldots]$ and $\mathbf{c}' = [-1, -1, 1, -1, \ldots]$ are sequences (or paths) of signs c_i indexed by $i = 0, \ldots, N$. The summation is taken over all possible combinations of $\mathbf{c}$ and $\mathbf{c}'$, representing distinct sign trajectories (paths) within the exponential.

In the continuum limit, the product becomes an integral in the exponent, leading to the following path-integral representation:

$$\frac{n(u)}{n_0} = \int \mathcal{D}[\mathbf{c}]\,\mathcal{D}[\mathbf{c}']\,A[\mathbf{c},\mathbf{c}']\exp\left[\int_0^u d\tilde{u}\left(\kappa(\tilde{u}) + \mathbf{c}(\tilde{u})\,\mathcal{K}_x(\tilde{u}) + \mathbf{c}'(\tilde{u})\,\mathcal{K}_y(\tilde{u})\right)\right], \tag{B4}$$

as discussed for Eq. (30).

The aforementioned path-integral formulation can be numerically approximated under a mean-field assumption by directly evaluating the defining expression,

$$\begin{aligned} n(\phi, \theta_0) &\approx \sum_{\mathbf{c},\mathbf{c}'} \exp\left[\sum_{i=0}^{\phi} \kappa(u_i)\,(x(\theta_{i+1}) - x(\theta_i) + y(\theta_{i+1}) - y(\theta_i))\right] \\ &\approx \exp\left[\kappa(\phi)\left(R(D_x)\,(x(\phi) - x(\theta_0)) + R'(D_y)\,(y(\phi) - y(\theta_0))\right)\right] \\ &\quad + \exp\left[-\kappa(\phi)\left(R(D_x)\,(x(\phi) - x(\theta_0)) + R'(D_y)\,(y(\phi) - y(\theta_0))\right)\right], \end{aligned} \tag{B5}$$

where $R(D_x)$ and $R'(D_y)$ are signed (parametrization-dependent) coefficients. In the last line, only two overall sign contributions are retained, consistent with the endpoint (mean-field) treatment of the path sum.

To obtain the ensemble-averaged density, we further sum over all possible starting points θ_j:

$$n(\phi) \approx \sum_{j=0}^{2\pi} n(\phi, \theta_j). \tag{B6}$$

These mean-field solutions are numerically demonstrated for circular and elliptical boundary fields, as presented in Figs. 3 and 4.

APPENDIX C: ELLIPTICAL BOUNDARY PARAMETRIZATION

Consider an isotropic diffusion setting with $D_x = D_y$ and an elliptical boundary confinement centered at the origin, characterized by a semimajor axis a and a semiminor axis b [as shown in Fig. 4(a)]. The boundary is parametrized by $\theta_0 \in [0, 2\pi)$, corresponding to a boundary point located at $[a\cos\theta_0,\ b\sin\theta_0]$.

For simplicity, we define the local configuration space using a second ellipse with the same aspect ratio, scaled by a global constant r, such that

$$\mathbf{r}_{\mathrm{bd}}(r, \phi, \theta_0) = a(r\cos\phi - \cos\theta_0)\,\hat{\mathbf{x}} + b(r\sin\phi - \sin\theta_0)\,\hat{\mathbf{y}}. \tag{C1}$$

The local curvature at the boundary point (i.e., when $r = 1$) takes the form

$$\kappa(\theta_0) = \frac{ab}{\left(b^2\cos^2\theta_0 + a^2\sin^2\theta_0\right)^{3/2}}. \tag{C2}$$

Analytical solutions of the adatom density field under the mean-field approximation [Eq. (B5)] show close agreement with the results obtained from direct simulations of adatom Langevin dynamics sampled via Langevin-based Monte Carlo simulations [Figs. 4(b) and 4(c)].

APPENDIX D: BOUNDARY-MEDIATED SEMIDETERMINISTIC QD PLACEMENTS UNDER DIFFERENT GEOMETRIES

As an extension of Fig. 7, we illustrate how variations in the elongated lozenge boundary field (aspect ratio a) affect the spatial QD distribution along the boundary

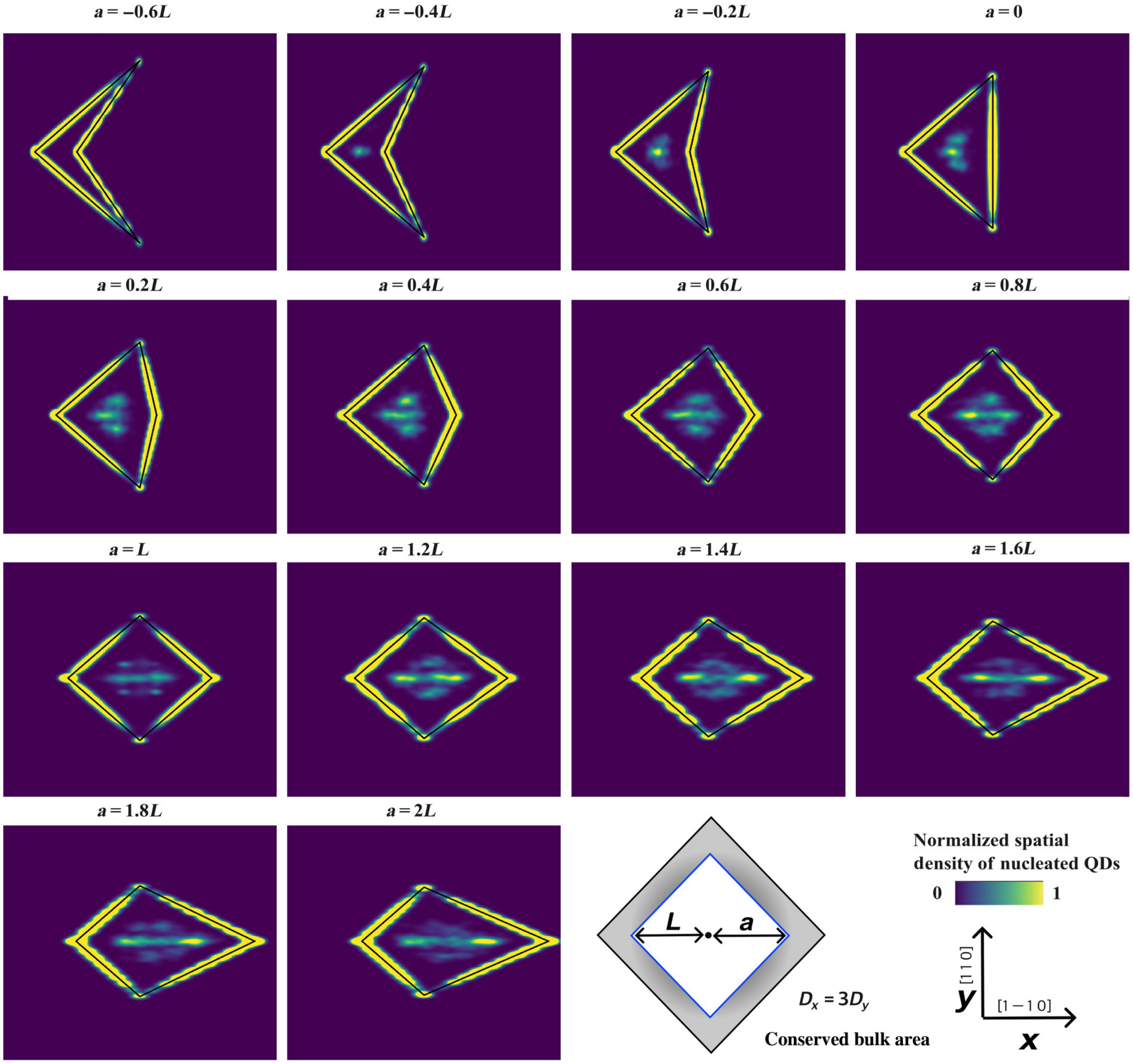

FIG. 8. Full parameter sweep over $a \in [-0.6L, 2L]$ for the elongated lozenge boundary field presented in Fig. 7. QD, quantum dot.

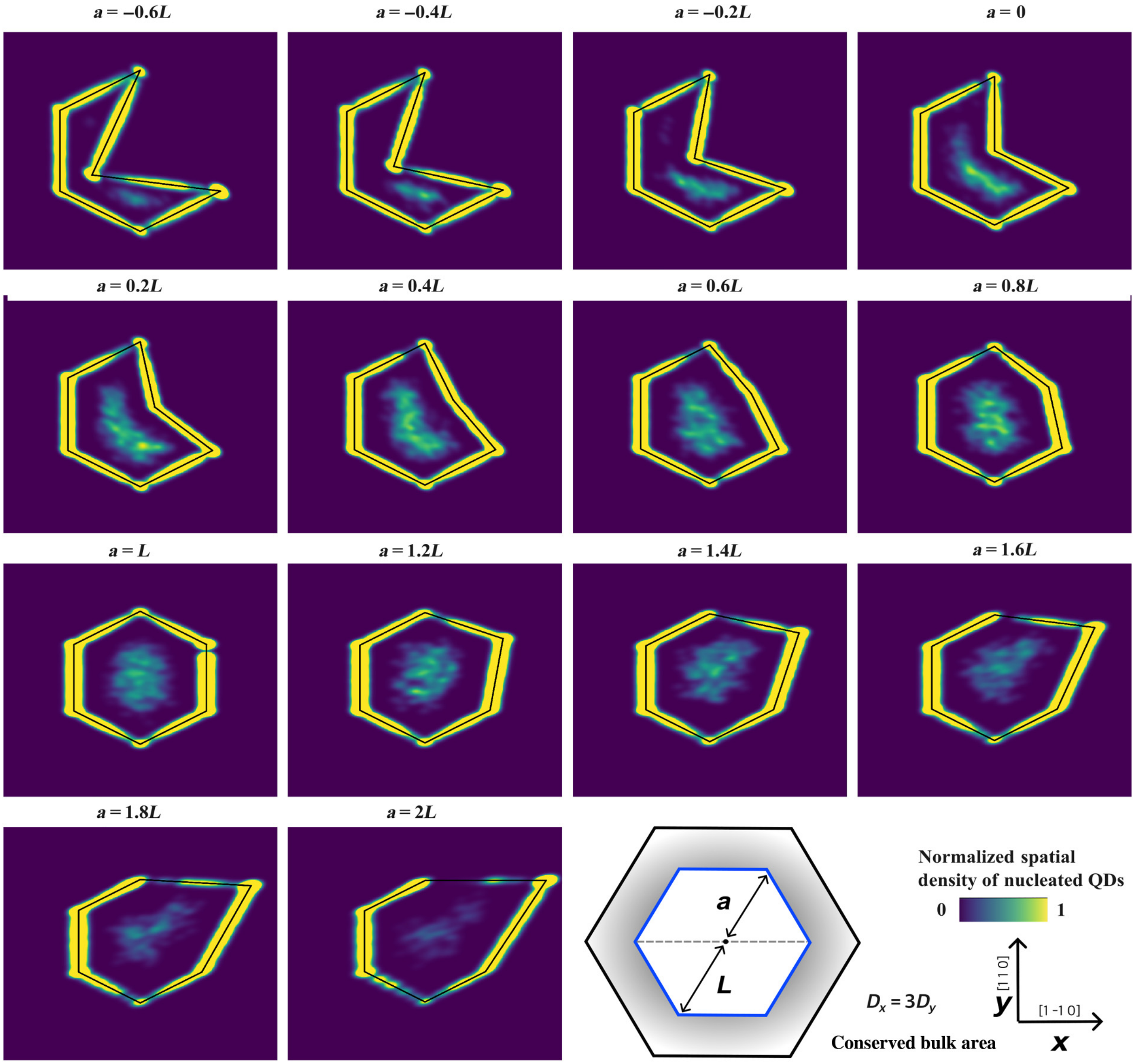

FIG. 9. Full parameter sweep over $a \in [-0.6L, 2L]$ for the hexagonal boundary field at 60° angle. QD, quantum dot.

contour and secondary nucleation statistics (Fig. 8). Negative a values produce compressed nucleation statistics with enhanced localization near the lozenge vertices along the fast diffusion axis, and increasing a elongates the secondary QD nucleation distribution. In contrast, due to flat edges, the hexagonal boundary field at a 60° angle (Fig. 9) exhibits weaker statistical localization than the lozenge geometries.

[1] T. Yoshie, A. Scherer, J. Hendrickson, G. Khitrova, H. Gibbs, G. Rupper, C. Ell, O. Shchekin, and D. Deppe, Vacuum Rabi splitting with a single quantum dot in a photonic crystal nanocavity, Nature **432**, 200 (2004).

[2] B. Ellis, M. A. Mayer, G. Shambat, T. Sarmiento, J. Harris, E. E. Haller, and J. Vuckovic, Ultralow-threshold electrically pumped quantum-dot photonic-crystal nanocavity laser, Nat. Photonics **5**, 297 (2011).

[3] S. Strauf, K. Hennessy, M. T. Rakher, Y. S. Choi, A. Badolato, L. C. Andreani, E. L. Hu, P. M. Petroff, and D. Bouwmeester, Self-tuned quantum dot gain in photonic crystal lasers, Phys. Rev. Lett. **96**, 127404 (2006).

[4] J. Reithmaier, G. Sek, A. Löffler, C. Hofmann, S. Kuhn, S. Reitzenstein, L. Keldysh, V. Kulakovskii, T. Reinecke, and A. Forchel, Strong coupling in a single quantum dot-semiconductor microcavity system, Nature **432**, 197 (2004).

[5] E. Peter, P. Senellart, D. Martrou, A. Lemaitre, J. Hours, J. M. Gérard, and J. Bloch, Exciton-photon strong-coupling regime for a single quantum dot embedded in a microcavity, Phys. Rev. Lett. **95**, 067401 (2005).

[6] S. Strauf, N. G. Stoltz, M. T. Rakher, L. A. Coldren, P. M. Petroff, and D. Bouwmeester, High-frequency single-photon source with polarization control, Nat. Photonics **1**, 704 (2007).

[7] H. Snijders, J. A. Frey, J. Norman, V. P. Post, A. C. Gossard, J. E. Bowers, M. P. van Exter, W. Loffler, and D. Bouwmeester, Fiber-coupled cavity-QED source of identical single photons, Phys. Rev. Appl. **9**, 031002(R) (2018).

[8] D. Najer, I. Sollner, P. Sekatski, V. Dolique, M. C. Lobl, D. Riedel, R. Schott, S. Starosielec, S. R. Valentin, A. D. Wieck, N. Sangouard, A. Ludwig, and R. J. Warburton, A gated quantum dot strongly coupled to an optical microcavity, Nature **575**, 622 (2019).

[9] H. J. Kimble, The quantum internet, Nature **453**, 1023 (2008).

[10] M. Atature, D. Englund, N. Vamivakas, S.-Y. Lee, and J. Wrachtrup, Material platforms for spin-based photonic quantum technologies, Nat. Rev. Mater. **3**, 38 (2018).

[11] C. L. Morrison, R. G. Pousa, F. Graffitti, Z. X. Koong, P. Barrow, N. G. Stoltz, D. Bouwmeester, J. Jeffers, D. K. L. Oi, B. D. Gerardot, and A. Fedrizzi, Single-emitter quantum key distribution over 175 km of fibre with optimised finite key rates, Nat. Commun. **14**, 3573 (2023).

[12] W. B. Gao, P. Fallahi, E. Togan, J. Miguel-Sanchez, and A. Imamoglu, Observation of entanglement between a quantum dot spin and a single photon, Nature **491**, 426 (2012).

[13] I. J. Luxmoore, N. A. Wasley, A. J. Ramsay, A. C. T. Thijssen, R. Oulton, M. Hugues, S. Kasture, V. G. Achanta, A. M. Fox, and M. S. Skolnick, Interfacing spins in an InGaAs quantum dot to a semiconductor waveguide circuit using emitted photons, Phys. Rev. Lett. **110**, 037402 (2013).

[14] J. R. Schaibley, A. P. Burgers, G. A. McCracken, L. M. Duan, P. R. Berman, D. G. Steel, A. S. Bracker, D. Gammon, and L. J. Sham, Demonstration of quantum entanglement between a single electron spin confined to an InAs quantum dot and a photon, Phys. Rev. Lett. **110**, 167401 (2013).

[15] C. Bonato, F. Haupt, S. S. R. Oemrawsingh, J. Gudat, D. Ding, M. P. van Exter, and D. Bouwmeester, CNOT and Bell-state analysis in the weak-coupling cavity QED regime, Phys. Rev. Lett. **104**, 160503 (2010).

[16] M. Kroutvar, Y. Ducommun, D. Heiss, M. Bichler, D. Schuh, G. Abstreiter, and J. Finley, Optically programmable electron spin memory using semiconductor quantum dots, Nature **432**, 81 (2004).

[17] Y. He, Y. M. He, Y. J. Wei, X. Jiang, K. Chen, C. Y. Lu, J. W. Pan, C. Schneider, M. Kamp, and S. Hoefling, Quantum state transfer from a single photon to a distant quantum-dot electron spin, Phys. Rev. Lett. **119**, 060501 (2017).

[18] C. Jennings, X. Ma, T. Wickramasinghe, M. Doty, M. Scheibner, E. Stinaff, and M. Ware, Self-assembled InAs/GaAs coupled quantum dots for photonic quantum technologies, Adv. Quantum Technol. **3**, 1900085 (2020).

[19] T. Heindel, J.-H. Kim, N. Gregersen, A. Rastelli, and S. Reitzenstein, Quantum dots for photonic quantum information technology, Adv. Opt. Photonics **15**, 613 (2023).

[20] M. L. Chan, A. Tiranov, M. H. Appel, Y. Wang, L. Midolo, S. Scholz, A. D. Wieck, A. Ludwig, A. S. Sorensen, and P. Lodahl, On-chip spin-photon entanglement based on photon-scattering of a quantum dot, NPJ Quantum Inf. **9**, 49 (2023).

[21] D. A. Gangloff, G. Ethier-Majcher, C. Lang, E. V. Denning, J. H. Bodey, D. M. Jackson, E. Clarke, M. Hugues, C. Le Gall, and M. Atature, Quantum interface of an electron and a nuclear ensemble, Science **364**, 62 (2019).

[22] P. Senellart, G. Solomon, and A. White, High-performance semiconductor quantum-dot single-photon sources, Nat. Nanotechnol. **12**, 1026 (2017).

[23] C. Schneider, A. Huggenberger, T. Suenner, T. Heindel, M. Strauss, S. Goepfert, P. Weinmann, S. Reitzenstein, L. Worschech, M. Kamp, S. Hoefling, and A. Forchel, Single site-controlled In(Ga)As/GaAs quantum dots: Growth, properties and device integration, Nanotechnology **20**, 434012 (2009).

[24] L. Sapienza, M. Davanco, A. Badolato, and K. Srinivasan, Nanoscale optical positioning of single quantum dots for bright and pure single-photon emission, Nat. Commun. **6**, 7833 (2015).

[25] I. Limame, C.-W. Shih, A. Koltchanov, F. Heisinger, F. Nippert, M. Plattner, J. Schall, M. R. Wagner, S. Rodt, P. Klenovsky, and S. Reitzenstein, Epitaxial growth and characterization of multi-layer site-controlled InGaAs quantum dots based on the buried stressor method, Appl. Phys. Lett. **124**, 061102 (2024).

[26] M. S. Solodovnik, D. V. Kirichenko, D. D. Dukhan, N. E. Chernenko, I. S. Makhov, N. A. Shandyba, M. M. Eremenko, N. V. Kryzhanovskaya, and S. V. Balakirev, New way to nanopattern GaAs surface for subcritical formation of InAs quantum dots, Appl. Surf. Sci. **688**, 162373 (2025).

[27] C. Shang, E. T. Hughes, M. R. Begley, R. Koscica, M. Fouchier, K. Feng, W. He, Y. Wan, G. Leake, P. Ludewig, and J. E. Bowers, Design rules for addressing material asymmetry induced by templated epitaxy for integrated heteroepitaxial on-chip light sources, Adv. Funct. Mater. **33**, 2304645 (2023).

[28] X. Zhao, W. Liu, Y. Bao, X. Chen, C. Ji, G. Yang, B. Wei, F. Yang, and X. Wang, Site-controlled growth of In(Ga)As/GaAs quantum dots on patterned substrate, Nanotechnology **36**, 052001 (2025).

[29] T. Nishinaga, in *Handbook of Crystal Growth*, edited by T. F. Kuech (North-Holland, Boston, 2015), 2nd ed., p. 943.

[30] N. Bart *et al.*, Wafer-scale epitaxial modulation of quantum dot density, Nat. Commun. **13**, 1633 (2022).

[31] B. Joyce, D. Vvedensky, A. Avery, J. Belk, H. Dobbs, and T. Jones, Nucleation mechanisms during MBE growth of lattice-matched and strained III-V compound films, Appl. Surf. Sci. **130-132**, 357 (1998); 4th International Symposium on Atomically Controlled Surfaces and Interfaces (ACSI 4), Tokyo, Japan, Oct. 27–30, 1997.

[32] V. Shchukin and D. Bimberg, Spontaneous ordering of nanostructures on crystal surfaces, Rev. Mod. Phys. **71**, 1125 (1999).

[33] N. Moll, M. Scheffler, and E. Pehlke, Influence of surface stress on the equilibrium shape of strained quantum dots, Phys. Rev. B **58**, 4566 (1998).

[34] Y. Berdnikov, P. Holewa, S. Kadkhodazadeh, J. M. Smigiel, A. Sakanas, A. Frackowiak, K. Yvind, M. Syperek, and E. Semenova, Near-critical Stranski-Krastanov growth of InAs/InP quantum dots, Sci. Rep. **14**, 23697 (2024).

[35] L. Nurminen, A. Kuronen, and K. Kaski, Kinetic Monte Carlo simulation of nucleation on patterned substrates, Phys. Rev. B **63**, 035407 (2000).

[36] D. Del Gaudio, L. K. Aagesen, S. Huang, T. M. Johnson, B. D. Faeth, H. Lu, R. M. Ziff, and R. S. Goldman, Influence of

surface nano-patterning on the placement of InAs quantum dots, J. Appl. Phys. **124**, 115307 (2018).

[37] A. Baskaran and P. Smereka, Mechanisms of Stranski-Krastanov growth, J. Appl. Phys. **111**, 044321 (2012).

[38] K. E. Sautter, K. D. Vallejo, and P. J. Simmonds, Strain-driven quantum dot self-assembly by molecular beam epitaxy, J. Appl. Phys. **128**, 031101 (2020).

[39] J. Venables, G. Spiller, and M. Hanbucken, Nucleation and growth of thin films, Rep. Prog. Phys. **47**, 399 (1984).

[40] C. Meyer, E. Cheng, and G. Triplett, Orientation-dependent pseudomorphic growth of InAs for use in lattice-mismatched mid-infrared photonic structures, J. Vac. Sci. Technol. B **32**, 02C118 (2014).

[41] J. Tersoff and R. M. Tromp, Shape transition in growth of strained islands—spontaneous formation of quantum wires, Phys. Rev. Lett. **70**, 2782 (1993).

[42] G. Costantini, A. Rastelli, C. Manzano, P. Acosta-Diaz, G. Katsaros, R. Songmuang, O. Schmidt, H. Von Känel, and K. Kern, Pyramids and domes in the InAs/GaAs(001) and Ge/Si(001) systems, J. Cryst. Growth **278**, 38 (2005); 13th International Conference on Molecular Beam Epitaxy (MBE XII), Edinburgh, UK, Aug. 22–27, 2004.

[43] J. Stangl, V. Holy, and G. Bauer, Structural properties of self-organized semiconductor nanostructures, Rev. Mod. Phys. **76**, 725 (2004).

[44] F. Long, S. P. A. Gill, and A. C. F. Cocks, Effect of surface-energy anisotropy on the kinetics of quantum dot formation, Phys. Rev. B **64**, 121307(R) (2001).

[45] I. Daruka and A. L. Barabasi, Dislocation-free island formation in heteroepitaxial growth: A study at equilibrium, Phys. Rev. Lett. **79**, 3708 (1997).

[46] M. Rosini, M. C. Righi, P. Kratzer, and R. Magri, Indium surface diffusion on InAs (2×4) reconstructed wetting layers on GaAs(001), Phys. Rev. B **79**, 075302 (2009).

[47] A. Kley, P. Ruggerone, and M. Scheffler, Novel diffusion mechanism on the GaAs(001) surface: The role of adatom-dimer interaction, Phys. Rev. Lett. **79**, 5278 (1997).

[48] M. Yamagiwa, T. Mano, T. Kuroda, T. Tateno, K. Sakoda, G. Kido, N. Koguchi, and F. Minami, Self-assembly of laterally aligned GaAs quantum dot pairs, Appl. Phys. Lett. **89**, 113115 (2006).

[49] H. Callen and T. Welton, Irreversibility and generalized noise, Phys. Rev. **83**, 34 (1951).

[50] H. Risken, *The Fokker-Planck Equation: Methods of Solution and Applications*, 2nd edition, Springer Series in Synergetics (Springer-Verlag, Berlin, 1996).

[51] C. B. Whitehead, S. Ozkar, and R. G. Finke, LaMer's 1950 model of particle formation: A review and critical analysis of its classical nucleation and fluctuation theory basis, of competing models and mechanisms for phase-changes and particle formation, and then of its application to silver halide, semiconductor, metal, and metal-oxide nanoparticles, Mater. Adv. **2**, 186 (2021).

[52] J. Tersoff and F. K. LeGoues, Competing relaxation mechanisms in strained layers, Phys. Rev. Lett. **72**, 3570 (1994).

[53] X. L. Li, G. Ouyang, and G. W. Yang, A thermodynamic theory of the self-assembly of quantum dots, New J. Phys. **10**, 043007 (2008).

[54] J. Wu and P. Jin, Self-assembly of InAs quantum dots on GaAs(001) by molecular beam epitaxy, Front. Phys. **10**, 7 (2015).

[55] A. Barabási, Thermodynamic and kinetic mechanisms in self-assembled quantum dot formation, Mater. Sci. Eng. B-Solid State Mater. Adv. Technol. **67**, 23 (1999); 1st Lawrence Symposium on Critical Issues in Epitaxy, Univ. Arizona, Ctr. Solid State Sci., Mesa, Arizona, USA, Jan. 06–09, 1999.

[56] H. M. Koduvely and A. Zangwill, Epitaxial growth kinetics with interacting coherent islands, Phys. Rev. B **60**, R2204 (1999).

[57] N. Kobayashi, T. Ramachandran, P. Chen, and A. Madhukar, *In situ*, atomic force microscope studies of the evolution of InAs three-dimensional islands on GaAs(001), Appl. Phys. Lett. **68**, 3299 (1996).

[58] M. Meixner, R. Kunert, and E. Schöll, Control of strain-mediated growth kinetics of self-assembled semiconductor quantum dots, Phys. Rev. B **67**, 195301 (2003).

[59] L. E. Shilkrot and D. J. Srolovitz, Adatom-step interactions: Atomistic simulations and elastic models, Phys. Rev. B **55**, 4737 (1997).

[60] T. Konishi, E. Clarke, C. W. Burrows, J. J. Bomphrey, R. Murray, and G. R. Bell, Spatial regularity of InAs-GaAs quantum dots: Quantifying the dependence of lateral ordering on growth rate, Sci. Rep. **7**, 42606 (2017).

[61] T. Mano, R. Nötzel, G. Hamhuis, T. Eijkemans, and J. Wolter, Formation of InAs quantum dot arrays on GaAs (100) by self-organized anisotropic strain engineering of a (In,Ga)As superlattice template, Appl. Phys. Lett. **81**, 1705 (2002).

[62] P. E. Vullum, M. Nord, M. Vatanparast, S. F. Thomassen, C. Boothroyd, R. Holmestad, B.-O. Fimland, and T. W. Reenaas, Quantitative strain analysis of InAs/GaAs quantum dot materials, Sci. Rep. **7**, 45376 (2017).

[63] X. Ding, Y. He, Z.-C. Duan, N. Gregersen, M.-C. Chen, S. Unsleber, S. Maier, C. Schneider, M. Kamp, S. Höfling, C.-Y. Lu, and J.-W. Pan, On-demand single photons with high extraction efficiency and near-unity indistinguishability from a resonantly driven quantum dot in a micropillar, Phys. Rev. Lett. **116**, 020401 (2016).

[64] L. Zhai, M. C. Lobl, G. N. Nguyen, J. Ritzmann, A. Javadi, C. Spinnler, A. D. Wieck, A. Ludwig, and R. J. Warburton, Low-noise GaAas quantum dots for quantum photonics, Nat. Commun. **11**, 4745 (2020).

[65] D. Cogan, Z.-E. Su, O. Kenneth, and D. Gershoni, Deterministic generation of indistinguishable photons in a cluster state, Nat. Photonics **17**, 324 (2023).

[66] H. Huet, P. R. Ramesh, S. C. Wein, N. Coste, P. Hilaire, N. Somaschi, M. Morassi, A. Lemaitre, I. Sagnes, M. F. Doty, O. Krebs, L. Lanco, D. A. Fioretto, and P. Senellart, Deterministic and reconfigurable graph state generation with a single solid-state quantum emitter, Nat. Commun. **16**, 4337 (2025).

[67] Z. Wang and D. Bouwmeester, Correspondence between quasiparticle dissipation and quantum information decay in open quantum systems, Phys. Rev. A **110**, 032407 (2024).

[68] A. B. A. Mohamed, H. Eleuch, and C. H. R. Ooi, Quantum coherence and entanglement partitions for two driven

quantum dots inside a coherent micro cavity, Phys. Lett. A **383**, 125905 (2019).

[69] J. Huang, A. Miranda, W. Liu, X. Cheng, B. Dwir, A. Rudra, K.-C. Chang, E. Kapon, and C. W. Wong, Spatial quantum-interference landscapes of multi-site-controlled quantum dots coupled to extended photonic cavity modes, Commun. Phys. **8**, 152 (2025).

[70] D. Loss and D. P. DiVincenzo, Quantum computation with quantum dots, Phys. Rev. A **57**, 120 (1998).

[71] Z. Wang, Semi-deterministic quantum dot placement in heteroepitaxy: Data, public archive, 2025, https://github.com/zhwangs/public-archive-Semi-Deterministic-Quantum-Dot-Placement-in-Heteroepitaxy.